Draft version February 1, 2017
Preprint typeset using LaTeX style AASTeX6 v. 1.0

arXiv:1701.08881v1 [astro-ph.HE] 31 Jan 2017

A *CHANDRA* X-RAY CENSUS OF THE INTERACTING BINARIES IN OLD OPEN CLUSTERS – COLLINDER 261

Smriti Vats[1] and Maureen van den Berg[2,1]
[1]Anton Pannekoek Institute for Astronomy, University of Amsterdam, Science Park 904, 1098 XH Amsterdam, The Netherlands; S.Vats@uva.nl
and
[2]Harvard-Smithsonian Center for Astrophysics, 60 Garden Street, Cambridge, MA 02138, USA; mvandenberg@cfa.harvard.edu

ABSTRACT

We present the first X-ray study of Collinder 261 (Cr 261), which at an age of 7 Gyr is one of the oldest open clusters known in the Galaxy. Our observation with the *Chandra X-ray Observatory* is aimed at uncovering the close interacting binaries in Cr 261, and reaches a limiting X-ray luminosity of $L_X \approx 4 \times 10^{29}$ erg s^{-1} (0.3–7 keV) for stars in the cluster. We detect 107 sources within the cluster half-mass radius r_h, and we estimate that among the sources with $L_X \gtrsim 10^{30}$ erg s^{-1}, ~26 are associated with the cluster. We identify a mix of active binaries and candidate active binaries, candidate cataclysmic variables, and stars that have "straggled" from the main locus of Cr 261 in the colour-magnitude diagram. Based on a deep optical source catalogue of the field, we estimate that Cr 261 has an approximate mass of 6500 $M_\odot$, roughly the same as the old open cluster NGC 6791. The X-ray emissivity of Cr 261 is similar to that of other old open clusters, supporting the trend that they are more luminous in X-rays per unit mass than old populations of higher (globular clusters) and lower (the local neighbourhood) stellar density. This implies that the dynamical destruction of binaries in the densest environments is not solely responsible for the observed differences in X-ray emissivity.

Keywords: open clusters and associations: individual (Collinder 261); X-rays: binaries; binaries: close; stars: activity; cataclysmic variables

1. INTRODUCTION

Open clusters with ages in excess of a few Gyr are relatively rare in the Galaxy (e.g. Kharchenko et al. 2013). Some aspect of their properties (perhaps their large initial mass or their location out of the Galactic plane, where they avoid interactions with large molecular clouds or the disruptive pull of external gravitational forces) helped them survive until old age. Studies of old open clusters, with their well-developed subgiant and giant branches, have been a cornerstone of stellar-evolution theory for many decades, thanks, in part, to their accurately measured ages and distances.

From the X-ray point of view, old open clusters are interesting for a number of reasons. First, X-ray observations efficiently detect different classes of close, interacting binaries, enabling the study of processes such as tidal coupling and the link between X-rays and rotation. The X-ray luminosity of late-type stars strongly depends on stellar rotation. As single stars age, they spin down due to magnetic braking (Pallavicini 1989). As a result, their X-ray emission decreases accordingly. An old star like our Sun (~4.5 Gyr) has an X-ray luminosity of about 10^{26} to 10^{27} erg s^{-1} (0.1–2.4 keV; Peres et al. 2000). Even with the deepest exposures of a sensitive X-ray telescope like the *Chandra X-ray Observatory*, this is nearly impossible to detect except for the nearest stars. Nevertheless, an early *ROSAT* observation of the old open cluster M 67, which lies at ~840 pc (Pasquini et al. 2008) and is about as old as the Sun (4 ± 0.5 Gyr; Dinescu et al. 1995), revealed a large number of X-ray sources among the cluster members (Belloni et al. 1993). Many of these turned out to be close, tidally interacting binaries where the stellar rotation is locked to the orbital period, and therefore kept at a level that can sustain magnetically active coronae. Subsequent *XMM-Newton* (Gondoin 2005; Giardino et al. 2008; Gosnell et al. 2012), and *Chandra* (van den Berg et al. 2004, 2013; Giardino et al. 2008) observations of old open clusters have detected many such active binaries (ABs). ABs can be binaries of two detached stars, or they can have a contact or semi-detached configuration such as in W UMa and Algol binaries, respectively. In terms of number of sources, ABs are the most prominent X-ray source class in old open clusters, but other classes of interacting binary are represented as well. In cataclysmic variables (CVs), the X-rays are the result of accretion from a late-type main-sequence donor onto a white dwarf. In fact, the first *ROSAT* observation of M 67 was aimed at studying the X-rays from a CV that was discovered in the optical (Gilliland et al. 1991). The origin of the X-ray emission from more exotic open-cluster binaries, like blue stragglers, is less well understood, but in X-rays they are more similar to the ABs than to the mass-transfer sources (van den Berg 2013).

A second motive for studying old open clusters in X-rays, is that their stellar densities lie in between those of the solar

neighbourhood ($\sim 0.1 M_\odot$ pc^{-3}) and dense globular clusters ($\geq 10^4 M_\odot$ pc^{-3}). This allows an investigation of the effect of stellar dynamics on the clusters' close-binary population, in a poorly studied density regime. With the growing sample of old open clusters studied in X-rays, it is now possible to do simple statistics regarding the number of sources detected in each source class. It was found that the number of CVs in M 67 and NGC 6791 scale with the present-day cluster mass, pointing at a primordial origin. For ABs, that proportionality is not so obvious, raising the issue of whether dynamical interactions that break up or create binaries, play a role (van den Berg et al. 2013). The expected low encounter rates in open clusters do not seem to favour the latter explanation. Nevertheless, there are clues that dynamical encounters shape the properties of at least some binaries. N-body models of M 67 (Hurley et al. 2005) suggest that primordial binaries *and* dynamical encounters are necessary to explain the blue-straggler population of M 67. Some individual systems, such as the likely triple S 1082 in M 67 (van den Berg et al. 2001; Sandquist et al. 2003) is also difficult to explain without invoking encounters. Therefore, the origin of the X-ray sources of old open clusters may not be solely primordial.

The X-ray emissivity, or the integrated X-ray luminosity per unit of mass, of globular clusters is lower than that of M 67 after removing the contribution from luminous low-mass X-ray binaries (LMXBs; e.g. Verbunt 2001). Ge et al. (2015) compared the X-ray emissivities of more diverse environments including dwarf elliptical galaxies and the local neighbourhood, and found that old open clusters also have higher X-ray emissivities than other old stellar populations. Various explanations have been suggested, relating to either the overall mass-loss history of the clusters, differences in dynamical encounter rates, or the processes underlying the X-ray emission. More study is needed to determine which of these factors are responsible.

In order to improve the census of X-ray sources in old open clusters, we are undertaking a survey with *Chandra* of open clusters with ages between 3.5 and 10 Gyr. The observations are designed to reach a limiting luminosity of $L_X \approx 10^{30}$ erg s^{-1} (0.3–7 keV), or better, at the distance of the clusters. As part of this survey, we have carried out the first X-ray study of Collinder 261 (Cr 261), and we present the results of our efforts in this paper. With an estimated age of 6–7 Gyr (Bragaglia & Tosi 2006), Cr 261 is one of the oldest open clusters in the Galaxy, being superseded in age by NGC 6791 (8–9 Gyr) and Berkeley 17 (8.5–10 Gyr) only. The cluster metallicity is close to solar (Drazdauskas et al. 2016), and reported values for the distance and reddening lie between 2.2–2.7 kpc and $E(B-V) \approx 0.25 - 0.34$, respectively (see e.g. Gozzoli et al. 1996, Carraro et al. 1999, Bragaglia & Tosi 2006), with a higher value of the reddening considered more plausible (Friel et al. 2003). In this paper, we adopt a distance of 2.5 kpc and $E(B-V) = 0.34$, unless stated otherwise. The latter corresponds to a V-band extinction $A_V = 1.05$ for the canonical ratio $A_V/E(B-V) = 3.1$, and a neutral hydrogen column density $N_H = 1.9 \times 10^{21}$ cm^{-2} (Predehl & Schmitt 1995). The Galactic coordinates of Cr 261 are $l = 301.7°$, $b = -5.5°$; due to its low Galactic latitude and location towards the bulge, the number of fore- and background stars projected onto the cluster is high. Cluster membership is poorly constrained for the majority of stars in the field. Cr 261 is included in the star cluster catalogue of Kharchenko et al. (2013), which lists structural parameters such as the overall size of the cluster and the radius of its central region. In this work, we present an estimate for the half-mass radius r_h and the approximate mass of Cr 261, which, to our knowledge, have not been reported in the literature before. These parameters facilitate a uniform comparison with the X-ray properties of other old Galactic clusters.

We present the X-ray and optical observations, and the data reduction in Sect. 2. In Sect. 3 we describe the analysis, which includes the creation of the X-ray and optical source catalogues, their cross-correlation to identify candidate optical counterparts to the *Chandra* sources, and the derivation of the structural properties of Cr 261. Sect. 4 is focused on the X-ray source classification. In Sect. 5 we discuss our results in the context of the X-ray emission from other old stellar populations, and we summarise our findings in Sect. 6.

2. OBSERVATIONS AND DATA REDUCTION

2.1. *X-ray Observations*

Cr 261 was observed with the Advanced CCD Imaging Spectrometer (ACIS; Garmire et al. 2003) on board *Chandra* starting 2009 November 9 14:50 UTC for a total exposure time of 53.8 ks (ObsID 11308). The observation was made in Very Faint, Timed exposure mode, with a single frame exposure time of 3.2 s. Kharchenko et al. (2013) estimate that the radius[1] of Cr 261 is ~14′.1. This is considerably larger than a single ACIS chip (8′.4×8′.4); therefore, we placed the centre of the cluster ($\alpha_{2000} = 12^h38^m06^s.0$, $\delta_{2000} = -68°22'01''$; Kharchenko et al. 2013[2]) close to the I 3 aimpoint, so that a larger contiguous part of the cluster could be imaged (see Figure 1). The CCDs used were I 0, I 1, I 2 and I 3 from the ACIS-I array, and S 2 and S 3 from the ACIS-S array.

We started the data reduction with the level-1 event file produced by the data processing pipeline of the *Chandra* X-ray Center and used CIAO 4.5 with CALDB 4.5.5.1 calibration files for further processing. To create the level-2 event file we used the `chandra_repro` script. A background light curve in the energy range 0.3–7 keV was created with the CIAO `dmextract` routine using source-free areas on the ACIS-I chips, and was analysed with the `lc_sigma_clip` routine. No background flares with more than 3σ excursions from the average background count rate were observed, hence the total

[1] Here we refer to the Kharchenko et al. (2013) parameter r_2, which is defined as the distance from the cluster centre where the projected stellar density drops to the average stellar density of the field.

[2] The cluster centre is redetermined in Sect. 3.3.

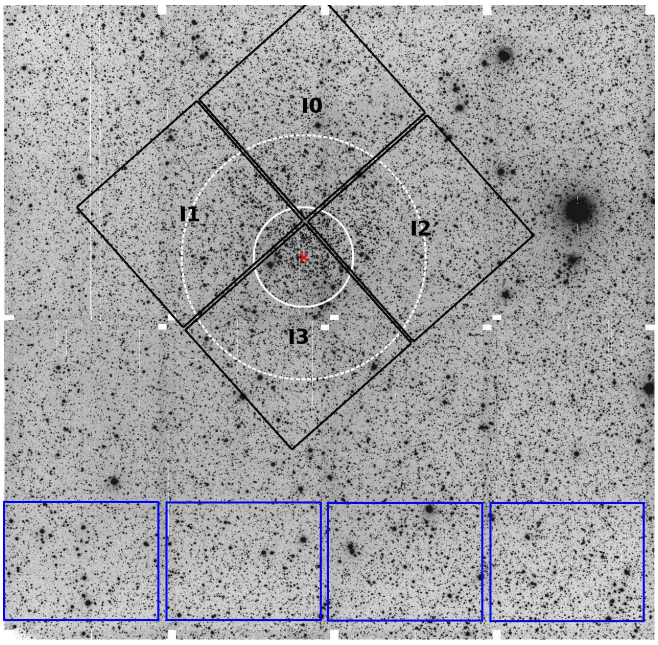

Figure 1. Stacked WFI *V*-band image of Cr 261. The four black squares show the ACIS-I field of view with chip IDs marked. The solid white circle marks the core radius of the cluster (r_c = 157″ ± 16″), centred on the cluster centre (marked by the red cross) as determined by us (see Sect. 3.3). The dashed white circle marks the half-mass radius of the cluster (r_h = 384″ ± 38″). Blue rectangles show the offset field used for determining the background stellar density. Small white rectangles are regions of zero optical exposure. North is up, east to the left.

exposure was used for further analysis.

2.2. *Optical Observations*

We retrieved optical images of Cr 261 in the *B* and *V* bands from the ESO public archive. These data were taken as part of the ESO Imaging Survey (EIS; program ID 164.O-0561). The observations of Cr 261 were made using the Wide Field Imager (WFI), mounted on the 2.2m MPG/ESO telescope at La Silla, Chile. The WFI has a field of view of 34′×33′ covered by a detector array of eight 2k×4k CCDs with a pixel scale of 0.″238 pixel^{-1}. The Cr 261 data were taken from 2001 June 27 23:55 UTC to 2001 June 28 00:38 UTC, with a total exposure time of 510 s in the *B* and *V* filter each. In each filter, two exposures of 240 s were taken, supplemented with a single short exposure of 30 s to get photometry for the bright stars. We only used the long exposures for our analysis. The seeing during the observations was ∼1.″15.

For reducing the optical images we used the Image Reduction and Analysis Facility (IRAF[3]) v2.16, supplemented by the MSCRED package for handling and reducing mosaic data. Basic data reduction steps of bias subtraction and flat-fielding were performed using the bias, and dome-and sky-flat images taken within one day of the science exposures. With the MSCCMATCH routine, the geometric distortion of the images was removed, and the eight individual chips of a given exposure were combined into a single image. We created a master *V*-band image by stacking the two individual, slightly offset, 240-s *V*-band exposures. As a result, in the stacked *V* image the space between the individual chips of the WFI mosaic (23″ wide along the length of the chips, and 14″ wide along their width) is largely, but not completely, filled in (see Figure 1). The stellar profiles in one of the *B*-band images of Cr 261 are very distorted, which prevented us from modelling a good PSF. Since this degrades the quality of the derived photometry, we opted to discard this low-quality image and use only a single 240-s *B* exposure for our analysis. Therefore, our *B*-band catalogue of the Cr 261 field has no coverage in the chip gaps.

[3] IRAF is distributed by the National Optical Astronomy Observatory, which is operated by the Association of Universities for Research in Astronomy (AURA) under a cooperative agreement with the National Science Foundation.

3. ANALYSIS

3.1. *X-ray Source Detection and Source Characterisation*

We limited the X-ray analysis to the data from chips I 0, I 1, I 2 and I 3. The S 2 and S 3 chips lie far from the I3 aimpoint, giving rise to large positional errors on any sources detected on them. Such large errors make it hard to identify optical counterparts, and thus to classify the sources.

Source detection was done in a soft (0.3–2 keV), hard (2–7 keV), and broad (0.3–7 keV) energy band. The CIAO source detection routine `wavdetect` was run for eight wavelet scales ranging from 1.0 to 11.3 pixels, each increasing by a factor of $\sqrt{2}$. Larger scales are better suited for more off-axis sources, where the PSF is wider or more distorted. Exposure maps were computed for an energy value of 1.5 keV. The `wavdetect` detection threshold (`sigthresh`) was set at 10^{-7}. The corresponding expected number of spurious detections per wavelet scale is 0.42 for all four ACIS chips combined, or 3.35 in total for all wavelet scales. We ran `wavdetect` for the three different energy bands and then cross-correlated the resulting source lists to obtain a master X-ray source list. We detected 113 distinct X-ray sources. To check if we had missed any real sources, we ran `wavdetect` again for a detection threshold of 10^{-6}, which increases the expected total number of spurious detections to 33.5. We found a total of 151 distinct X-ray sources with more than two counts (0.3–7 keV) in this case. The positions of seven of the extra 38 sources are found to match those of short-period binaries discovered by Mazur et al. (1995) (see Sect. 3.4). Close, interacting binaries are plausible real X-ray sources and indeed the expected number of chance alignments between the *Chandra* detections and the binaries in the Mazur catalogue is very low (Sect. 3.5). It is therefore likely that at least these seven additional sources are real; but given the ∼34 spurious detections that are expected, we do not believe that there are many

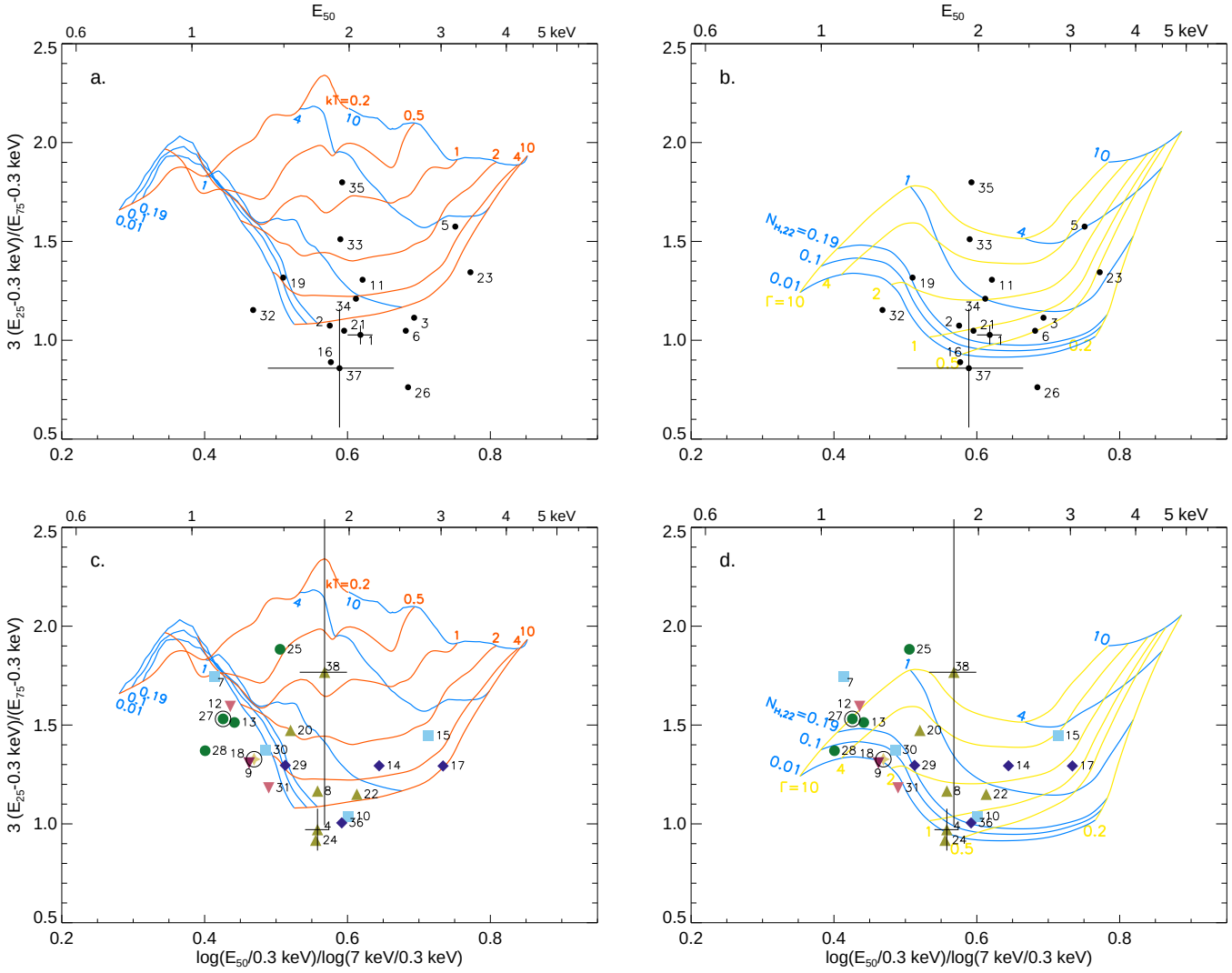

Figure 2. Quantile diagrams with model grids representing a MeKaL plasma (left) and a power-law spectrum (right). The top panels show sources *without*, and the bottom panels show sources *with* candidate optical counterparts (see Table 2 for their classification). The plasma temperature kT or photon index Γ, and the column density N_H can be estimated from the location of a source with respect to the grid: blue curves represent lines of constant N_H normalised in units of 10^{22} cm^{-2} ($N_{H,22}$, where $N_{H,22} \approx 0.19$ cm^{-2} is the cluster value), whereas orange curves are lines of constant kT (labeled in units of keV; left), and yellow curves are lines of constant Γ (right). The median energy E_{50} can be read off from the top x-axis. Here we show sources with twenty net counts (0.3–7 keV) or more; error bars are shown only for the sources with the highest and lowest number of counts in a given panel. Filled coloured symbols mark X-ray sources for which we have found candidate optical counterparts. Among them, green circles represent ABs and candidate ABs (Sect. 4.1), olive triangles are for candidate CVs or AGNs (Sect. 4.2), yellow four-point stars for candidate BSSs, pale red downward triangles for candidate SSGs, maroon downward triangles for candidate YSS (Sect. 4.3), pale blue squares for likely non-members of the cluster (Sect. 4.4), and deep blue diamonds for sources with uncertain classification (Sect. 4.5). Furthermore, sources CX 18 and CX 27 that have close-binary counterparts (Mazur et al. 1995) are marked with a larger black open circle.

more real sources among the extra detections. We flagged the sources that are only found for `sigthresh`=10^{-6}, but kept them in the master source list.

For computing the positional uncertainties, required for cross-correlation with other source catalogues, we used Eq. 5 from Hong et al. (2005), which gives the 95% confidence radius on the `wavdetect` position, P_{err}. The `wavdetect` routine provides us with the source positions, but is not optimised to measure source counts. We determined the net source counts using ACIS Extract (Broos et al. 2010, version 2013mar6). All events between 0.3 and 7 keV were extracted from regions enclosing ∼90% of the PSF at 1.5 keV. ACIS Extract also performs variability characterisation based on a Kolmogorov-Smirnov (K-S) test on the event arrival times for

sources with five counts or more that spend more than 90% of the total exposure time on the ACIS-I chips[4]. For example, a source near a chip edge could effectively have a shorter exposure time if the telescope dither motion occasionally moves it off the detector. There were 76 sources with no evidence for variability ($0.05 < P_{KS}$); four sources which showed possible variability ($0.005 < P_{KS} < 0.05$; CX 9, CX 13, CX 64, CX 93) and four which were likely variable ($P_{KS} < 0.005$; CX 63, CX 91, CX 120, CX 137), where P_{KS} is the probability for a source to have a constant count rate. The X-ray light curves of the variables suggest flare-like behaviour, with a large fraction of the total events arriving in a relatively short time interval. The brightest of these sources is CX 63, for which thirteen of seventeen events arrive in the last 3.5 h of the observation (and nine of seventeen events in a single hour). For the other three sources, 80% or more of the events arrive within 2.5–3 h. X-ray flares are commonly observed in active late-type stars or binaries. This is consistent with our classification of CX 120 (a W UMa binary and likely non-member of the cluster) and CX 91 and CX 137 (likely foreground late-type dwarfs). The classification of CX 63 is less secure, but it could be a late-type star or binary as well. These sources are further discussed in Sects. 4.4 and 4.5.

Only five sources in our catalogue have more than 100 net counts (0.3–7 keV), with the brightest source having 475 net counts. For the majority of our sources the spectrum of the X-ray emission is therefore poorly constrained. We calculated unabsorbed flux values in the 0.3–7 keV band, $F_{X,u}$, for each source from its net count rate and local `rmf` and `arf` response files using `Sherpa`. We assumed a 2 keV MeKaL model (*xsmekal*) attenuated by a neutral hydrogen column density $N_H = 1.9 \times 10^{21}$ cm^{-2} (the value for Cr 261) using the *xstbabs* model. The MeKaL model describes the emission from a hot, diffuse gas or optically thin plasma, as is appropriate for ABs. Since the nature of our sources is unknown a priori, and the number of counts is too low to do any detailed spectral fitting, we explored the effect of using different spectral models on the derived values of $F_{X,u}$. We compared the unabsorbed flux values obtained using the 2 keV MeKaL model with those obtained using a 1 keV MeKaL model, a 10 keV thermal bremsstrahlung model (*xsbrems*) and a power-law model (*xspowerlaw*) with a photon index, Γ, set to 1.4; the *xstbabs* model was used in all cases. The flux values obtained using these models were about 6% smaller, 40% larger, and 80% larger, respectively, than the flux value obtained using the 2 keV MeKaL model. The X-ray sensitivity limit, as defined by the unabsorbed flux of the faintest detection, was found to be $\sim 6 \times 10^{-16}$ erg cm^{-2} s^{-1} for the 2 keV MeKaL model and assumed cluster N_H, which corresponds to an X-ray luminosity of $L_X \approx 4 \times 10^{29}$ erg s^{-1} (0.3–7 keV) at the adopted cluster distance (2.5 kpc).

[4] based on the evaluation of the FRACEXPO keyword generated by `mkarf` in CIAO

In order to characterise the spectral properties of our X-ray sources we use quantile analysis, which is optimised for sources with few counts (Hong et al. 2004). In this method, the median energy, E_{50}, and 25% and 75% quartile energies (E_{25} and E_{75}, respectively) of the source events' energy distribution are used to determine spectral hardness and spectral shape. Conventional X-ray hardness ratios use fixed energy values for defining hard and soft energy bands, and give results of little meaning if all events lie in either the soft or the hard energy band. Details of the source properties are presented in Table 1, while quantile diagrams are shown in Figure 2 for sources with ≥ 20 net counts (0.3–7 keV).

3.2. *Optical Source Catalogue*

The absolute astrometry of the optical images was tied to the International Celestial Reference System (ICRS). We did this by computing an astrometric solution based on the positions of unsaturated stars in the field that are also included in the USNO CCD Astrograph Catalog 4 (UCAC4; Zacharias et al. 2013). For the V image we used 1912 unsaturated stars and obtained rms residuals of 0.″141 in right ascension and 0.″166 in declination in the solution. For the B image, we used 1773 unsaturated stars and obtained residuals of 0.″157 in right ascension and 0.″173 in declination.

For performing photometry, we used the `DAOPHOT` package in IRAF. After creating a source catalogue for the B and the V image separately, we cross-matched each of them with the Gozzoli et al. (1996) catalogue in order to convert our instrumental magnitudes to the Gozzoli et al. calibrated magnitudes in the Johnson system. The Gozzoli study covers a region of radius 3.′5 around their adopted cluster centre. We found 2018 matches for the sources in the B catalogue within a calibrated-magnitude range $13.7 < B < 24.0$, and 2276 matches for the V catalogue within a range of $13.0 < V < 22.5$. We manually inspected all the matched sources and found that none appeared to be blended or saturated. Over these magnitude ranges, a constant offset provides a good transformation from instrumental to calibrated magnitudes. The resulting WFI source lists for the entire field have a calibrated magnitude range of 12.9–23.5 in V and 13.7–24.6 in B. Finally, we cross-matched the B and V source lists to make a master optical source list. Some sources in the master catalogue were detected in the V band but were not present in the single B image due to its chip gaps and a shorter exposure.

The colour-magnitude diagram (CMD) of Figure 3 shows our B and V photometry of stars inside r_h (see next section).

3.3. *Estimate for the Half-mass Radius and Mass of Cr 261*

One of our aims is to compare the number of X-ray sources in Cr 261 with those detected in other old open clusters and globular clusters. Making a uniform comparison between clusters requires an estimate for their masses and structural parameters. An estimate for the King-profile (King 1962) core radius r_c of Cr 261 was derived by Froebrich et al.

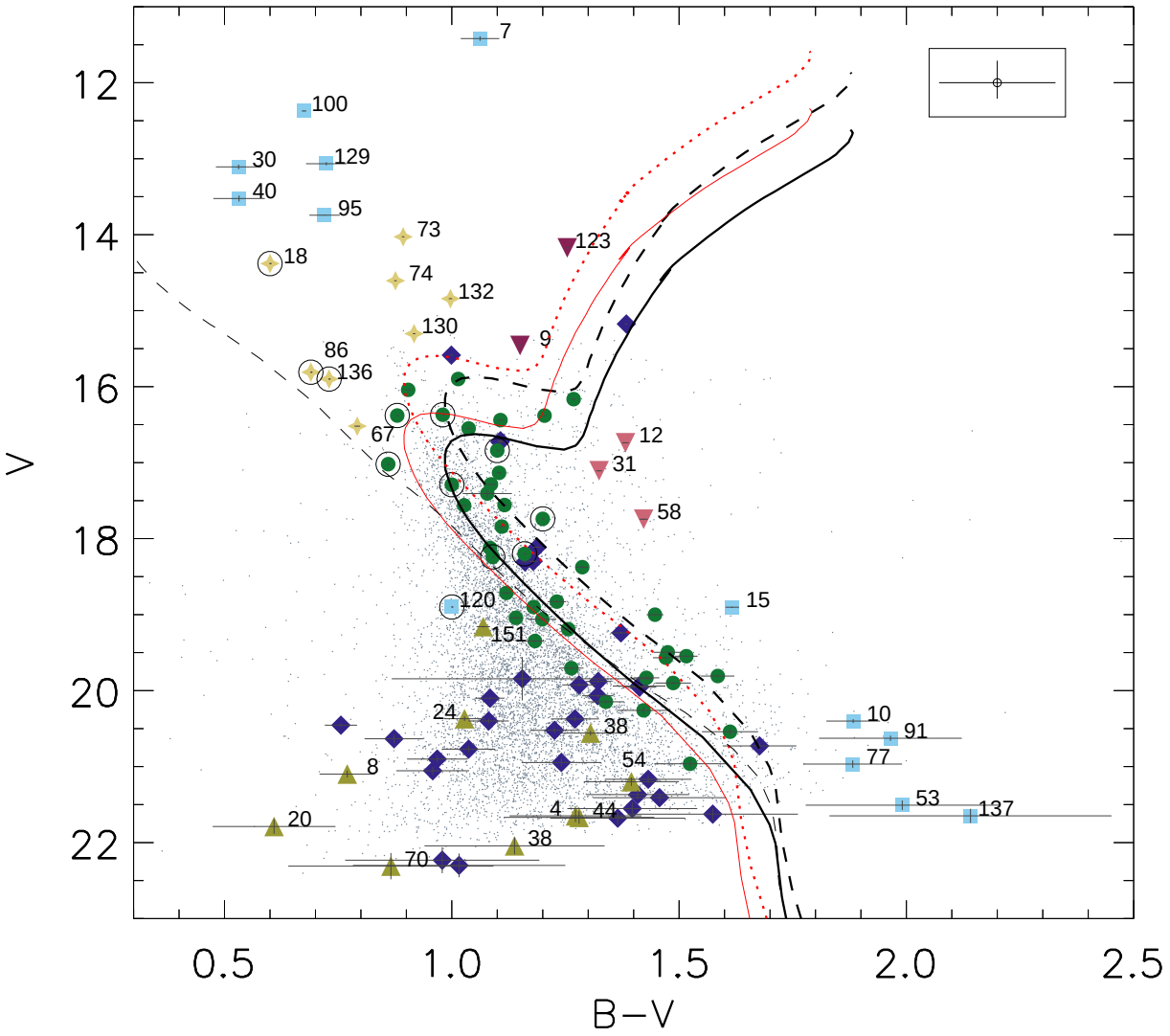

Figure 3. Colour-magnitude diagram of Cr 261 based on the WFI photometry. The different symbols and colours have the same meaning as in Figure 2. Furthermore, sources with close-binary counterparts are circled with a larger black open circle; for these stars, the *BV* photometry is obtained from (Mazur et al. 1995, see Sect. 4.1). Solid lines represent isochrones (Bressan et al. 2012; Chen et al. 2014; Tang et al. 2014; Chen et al. 2015) for the upper and lower limits of the cluster reddening (red for $E(B-V)_{low}$ = 0.25, and black for $E(B-V)_{up}$ = 0.34). Dotted lines are the same isochrones but shifted upward by −0.75 mag to indicate the limit for unresolved photometric binaries. The dashed line represents a zero-age main-sequence isochrone. Error bars are smaller than the symbols for some sources. The combined uncertainty in the location of the isochrone due to reddening and distance uncertainties is shown in the rectangle at the top right. For clarity, the ABs and uncertain classifications have not been labeled.

(2010) and Kharchenko et al. (2013), who found two significantly different values, viz. 52″ and 192″±48″, respectively. These values are based on the 2MASS near-infrared catalogue (Skrutskie et al. 2006), and (in case of Kharchenko et al. only) the optical PPMXL catalogue (Röser et al. 2010). Both star lists are relatively shallow, reaching ≲1 mag below the Cr 261 main-sequence turnoff. At the same time, the PPMXL proper motions in the field of Cr 261 (used by Kharchenko et al. to weed out possible non-members) have relatively large errors (∼9 mas yr^{-1}, on average) and do not display a clear distinction between cluster stars and field stars. We decided to derive our own estimate of r_c and r_h, without making use of the PPMXL proper motions.

In order to estimate r_h for Cr 261, we assumed that the

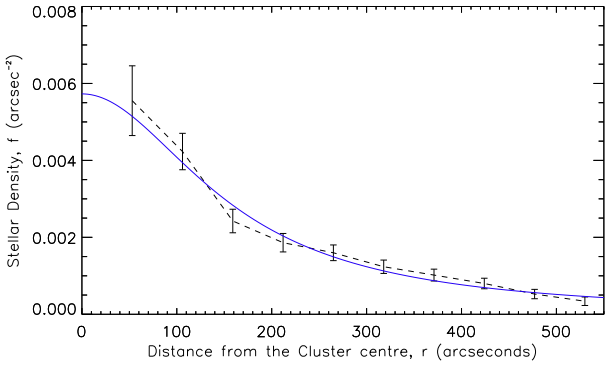

Figure 4. Projected stellar density profile of Cr 261 after correction for the contribution from foreground and background stars (points connected with a dashed line). The solid blue line shows the best-fitting King profile (King 1962), which has a central stellar density $f_0 = 0.0057 \pm 0.0007$ stars per arcsecond^2 and a core radius $r_c = 157'' \pm 16''$.

stars are symmetrically distributed about the cluster centre according to a King profile. In Figure 4 we plot the projected stellar density $f(r)$ versus radial offset from the cluster centre r, computed in 50″-wide annular regions around the centre. Stars were selected from the region between two 7-Gyr isochrones of solar metallicity ($Z = 0.019$; Bressan et al. 2012). One is modified for a distance of 2.5 kpc and reddened by $E(B-V) = 0.34$; the second isochrone is the same, but shifted upward in the CMD by –0.75 mag. This is done to include the contribution from unresolved photometric binaries (see Figure 3). To correct for the contribution from stars that are unrelated to the cluster, we estimated the density of stars within the same magnitude and colour limits, from a catalogue we created from offset fields in our WFI image (the blue rectangles in Figure 1) that lie outside the cluster radius r_2 (Kharchenko et al. 2013). We fitted the function $f(r) = f_0(1 + (r/r_c)^2)^{-1}$ to this background-corrected radial profile; here f_0 is the central projected stellar density. This function is the limit of the King profile for the assumption that the tidal radius r_t is much larger than r_c. In the case of Cr 261, the values of $r_c \approx 0.'8$ and $r_t \approx 22.'2$ as derived by Kharchenko et al. (2013), support this assumption. Fitting the above function to the radial-density profile, gives us a centre for the cluster that is about 1.′5 different from the one given by Kharchenko et al., viz. $\alpha_{2000} = 12^{\rm h}38^{\rm m}07^{\rm s}.1$, $\delta_{2000} = -68°23'33''$, with a formal uncertainty of about 16″. We have used this new cluster centre for all purposes in this study. The best-fitting King profile has $r_c = 157'' \pm 16''$, consistent with the value from Kharchenko et al. Adopting this value of r_c and assuming that the total mass of the cluster is contained within r_2, we used Eq. A3 in Freire et al. (2005) to compute r_h. We find that $r_h = 384'' \pm 38''$.

We estimated the mass of Cr 261 from the integrated V magnitude $I(V)$ of the cluster, following the method of Bellazzini et al. (2008). We calculated the integrated magnitude of stars inside r_h (i.e. $I_h(V)$) by summing the V-band fluxes of the stars inside r_h that satisfy the same magnitude and colour restrictions as outlined above. Again, photometry of the offset fields provides a correction for the flux density of foreground and background stars. We converted $I_h(V)$ to the absolute integrated V magnitude of stars inside r_h, which resulted in $M_h(V) \approx -3.6$. Next, we compared this value with the theoretical curves for the evolution in time of the absolute V magnitude of solar-metallicity star clusters of various, constant, masses (Bellazzini et al. 2008; Bragaglia et al. 2012). The age of Cr 261 (7 Gyr) combined with our estimate for $M_h(V)$, yields an approximate value for *half* the cluster mass of 4000–5500 $M_\odot$. The uncertainty stems from the range spanned by the theoretical curves computed for different initial-mass functions. As a final step, we have reduced the inferred total mass (about 8000–11 000 $M_\odot$) with an empirical scaling factor. This was motivated by our finding that the above method overestimates the masses of the old open clusters M 67 (by a factor 1.1–1.7) and NGC 188 (by a factor of 1.3–1.9), for which accurate virial masses have been determined (Geller et al. 2008, 2015). After scaling, our estimate for the *total* mass of Cr 261 is about 5800–7200 $M_\odot$.

Obviously, our mass estimate should be considered as approximate, only: we assumed that the total cluster mass is contained within Kharchenko et al.'s cluster radius r_2, we have no comprehensive list of members, and the evolutionary sequences for $M(V)$ from Bellazzini et al. (2008) may not be a perfect match to Cr 261 (in metallicity or mass function). For our purposes, though, this estimate is good enough.

3.4. *Optical and X-ray Cross-matching*

The possible error in the alignment of *Chandra's* absolute astrometry to the ICRS is small[5], but still allows for a systematic offset between the X-ray positions and our ICRS-calibrated optical positions. This systematic offset, or boresight, can be comparable in size to the random errors on the X-ray positions (P_{err}), and can complicate the search for optical counterparts if not corrected for. To calculate the boresight, we used the 45 short-period ($P < 3$ d) close binaries that were discovered by Mazur et al. (1995) in an optical-variability study of the Cr 261 field. The reason for using the short-period variables for calculating the boresight is that close binaries are plausible X-ray emitters and hence, there is a lower chance of spurious detections that could affect the boresight measurement (see also Sect. 3.5). With the finding charts in Mazur et al., we were able to identify all 45 variables among the WFI sources. Their WFI positions were then cross-matched with the X-ray catalogue, where we adopted a 95% match radius that combines the error in the optical po-

[5] For ACIS-I, the 95% confidence radius on the alignment is ~0.′9–1″ within a distance of 3′ from the aimpoint; see http://cxc.harvard.edu/cal/ASPECT/celmon

sitions[6] and the random error on the X-ray positions (P_{err}) in quadrature. To account for errors in the alignment, we also add the 95% confidence radius on *Chandra's* absolute astrometry. Fifteen candidate counterparts were thus found, which were then used to calculate the boresight from the average X-ray–optical positional offsets. After updating the X-ray positions for this initial boresight, the cross-matching was repeated until the net boresight converged. This method for calculating and correcting for the boresight is outlined in detail in Sect. 3.3.1 of van den Berg et al. (2013). We found a small boresight that is consistent with zero, viz. 0.″06±0.″07 in right ascension and 0.″09±0.″08 in declination.

After correcting the X-ray source positions for the (almost negligible) boresight, we matched our X-ray source list with the entire optical source list, again using 95% match radii. For 89 unique X-ray sources, we found 124 optical matches; of the latter, 104 are present in both the *V* and *B* images while for 20 we only have a *V* or *B* detection. We also inspected the area around each X-ray source in the WFI images by eye, and discovered that five more X-ray sources have candidate optical counterparts that are saturated and therefore missing from our optical catalogue. Finally, we added to the list of candidate counterparts six optical sources that lie just outside the 95% match radius, but inside the 3-σ radius. In total, 98 of the 151 unique X-ray sources were thus matched to one or more optical sources. For a complete list of candidate counterparts and their optical properties we refer to Table 2.

3.5. *False Positives Test, Background Galaxies, and Galactic Sources*

To estimate the number of spurious matches between our X-ray and optical sources, we calculated the surface density of optical sources. Within r_c, the average density is 0.029 sources arcsec^{-2}, while between r_c and r_h it drops slightly to 0.024 sources arcsec^{-2}. Multiplying the optical source densities with the total area covered by the 95% error circles of the X-ray sources in the two regions, we expect 2.4 spurious matches among the 23 matches that we find in this central region, and 11.6 spurious matches among the 47 matches in the outer region. Similarly, we use the number of Mazur variables per arcsec^2 to estimate that the number of spurious matches between X-ray sources and variables is 0.021 out of seven matches in the inner region, and 0.022 out of seven matches for the outer region (one X-ray–detected Mazur variables lies outside r_h). Therefore, all Mazur binaries that match with a *Chandra* source are likely real counterparts.

In order to estimate the number of background galaxies N_B among our X-ray detections, we used the relation for the cumulative number density of high–galactic-latitude X-ray sources above a given flux limit S (Eq. 5 in Kim et al. 2007). We adopted the $\log N_B - \log S$ relation for the 0.3–8 keV band, which of the energy ranges considered in the Kim study is closest to our broad band (0.3–7 keV). To convert counts to fluxes we adopted a power-law spectrum with $\Gamma = 1.4$ and $N_H = 2.3\times10^{21}$ cm^{-2}, i.e. equal to the total integrated Galactic column density along the line of sight (Marshall et al. 2006). We calculated N_B for $r < r_c$, where most X-ray sources that are truly associated with Cr 261 are expected to lie. The reason is that closer to the centre, the density of cluster stars is simply higher; in addition, mass segregation makes the radial distribution of binaries (and thus potential X-ray sources) more concentrated. For a 5-count detection limit, we expect $N_B \approx 9.5 \pm 3.1$ versus 22 sources actually detected. For a 10-count limit, it is expected that $\sim 5.7 \pm 2.4$ of the ten sources detected are extra-galactic. In the region $r_c < r \leq r_h$, 45.7±6.8 of the 58 sources detected above 5 counts, or 27.3 ± 5.2 of the 38 sources detected above 10 counts are expected to be extra-galactic. These numbers indicate that we do detect a population of, mainly faint, X-ray sources that is truly associated with the cluster.

Given the low Galactic latitude of Cr 261, a few foreground X-ray sources are also expected to contaminate our sample. The exact number is hard to estimate since there is no Galactic X-ray source density distribution for this latitude that reaches down to our detection limit. We have used the $\log N - \log S$ curves from Figure 9 in Ebisawa et al. (2005) for the soft band (0.5–2 keV), and read off the $\log N$ for a flux limit that corresponds to a 5-count detection emitting a 2 keV MeKaL spectrum and $N_H = 1.9 \times 10^{21}$ cm^{-2}. We expect ∼2.0 Galactic sources in the region inside r_c and ∼8.2 sources in the $r_c < r < r_h$ annulus; this must be an upper limit since the Ebisawa field lies right in the plane while Cr 261 is a few degrees off. Other factors, such as the difference between our and Ebisawa's soft band, and uncertainties in the X-ray spectral model and N_H, also affect the accuracy of this number.

4. RESULTS

We used three criteria to classify our X-ray sources. First, we considered the hardness of the X-ray spectrum as inferred from the energy quantiles. Coronally active stars and binaries have thermal X-ray spectra with plasma temperatures that generally do not exceed 3 – 4 keV (e.g. Güdel 2004). The integrated Galactic column density in the direction of Cr 261 is $\sim 2.3 \times 10^{21}$ cm^{-2}; Galactic X-ray sources without any intrinsic absorption should therefore have an N_H not larger than this. As a result of these temperature and N_H constraints, the expected E_{50} values for coronal sources are not much higher than ∼1.5 keV[7]. On the other hand, accreting binaries with compact objects, and AGNs often have intrinsically harder X-ray spectra, and sometimes are observed through additional, localised obscuring material; in both cases, the expected E_{50} is higher than ∼1.5 keV.

[6] The errors on the optical positions that are adopted here are the 1-σ errors in the astrometric calibration given in Sect. 3.2, scaled to a 95% confidence radius assuming a 2-D gaussian error distribution

[7] In the MeKal grid of Figures 2a and 2c, the location $kT \approx 4$ keV and $N_H \approx 2 \times 10^{21}$ cm^{-2} corresponds to $E_{50} \approx 1.5$ keV (see top axes).

Secondly, we looked at the ratio of the unabsorbed X-ray to optical flux, or the limits thereon for sources without candidate optical counterparts. We calculated this ratio with the equation $\log(F_X/F_V)_u = \log F_{X,u} + V_0/2.5 + 5.44$, where the last term is the logarithm of the V-band flux for sources with $V = 0$. We adopted a 2 keV MeKaL model to calculate X-ray fluxes, assumed $N_H = 1.9 \times 10^{21}$ cm^{-2} to correct for absorption, and used $V_0 = V - A_V = V - 1.05$. We caution that for most sources, N_H is unknown; if the adopted N_H is lower (higher) than the actual N_H, the flux ratio is overestimated (underestimated). Like E_{50}, the flux ratio is mostly useful to distinguish between coronal and accretion-powered sources. The former typically have $\log(F_X/F_V)_u \lesssim -1$, with the most active late-type dwarfs reaching values of about -0.5, while the latter have $\log(F_X/F_V)_u \gtrsim -1$ (Stocke et al. 1991). Indeed, for our sources, the average flux ratio is lower for soft ($E_{50} \lesssim 1.5$ keV) than for hard ($E_{50} \gtrsim 1.5$ keV) sources (Figure 5). An optical source inside the X-ray error circle is not necessarily the true counterpart, but can be a spurious match. Finding a relatively hard X-ray source with a low $\log(F_X/F_V)_u$ value, can signal such a random alignment.

For sources with candidate optical counterparts we also took into account the position of these matches in the CMD. In most cases, this works reasonably well to separate ABs from AGNs (which can lie far off the cluster sequence) and CVs (which typically are blue). The position in the CMD does a poor job in separating cluster stars from fore- or background stars. As can be seen in Figure 3, and also in the CMDs in Gozzoli et al. (1996), the cluster stars do not clearly stand out. The lack of membership information for stars in the field of Cr 261 limits the classification of our *Chandra* sources, as we discuss below. In the following, X-ray fluxes and luminosities refer to the 0.3–7 keV band.

4.1. *Active Binaries and Candidate Active Binaries*

For identifying possible ABs in Cr 261, we selected sources with candidate optical counterparts that lie along the cluster main sequence or sub-giant branch; if a source has multiple matches that all satisfy this condition, it is also classified as a (candidate) AB. We allowed for the possible contribution to the light by a binary companion, and for uncertainties in the reddening, as indicated by the pairs of black and red isochrones in Figure 3. The uncertainty in the cluster distance (~350 pc, based on the range of distances reported in the literature), and in our absolute photometric calibration (Sect. 3.2) are also sources of systematic error (see the error bar in the top right of Figure 3). Therefore, we classified candidate matches that are only a little bit off the main sequence or sub-giant branch as ABs, too.

A total of 33 *Chandra* sources satisfy the photometric criteria outlined above *and* have E_{50} values within 1σ of 1.5 keV or lower; all have $\log(F_X/F_V)_u \lesssim -1.4$. We classified them as "AB" in Table 2. Four additional sources (CX 62, CX 80, CX 115, CX 125) have similar optical and X-ray properties,

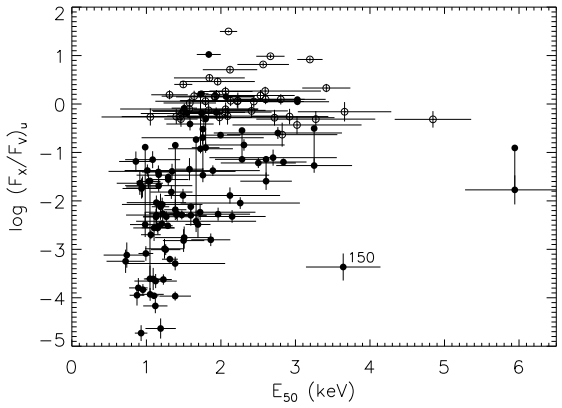

Figure 5. The median energies E_{50} and X-ray–to–optical flux ratios $\log(F_X/F_V)_u$ show a trend of lower flux ratios for soft sources than for harder sources. For sources without optical counterparts, the lower limit on $\log(F_X/F_V)_u$ (shown as open circles) was calculated for the detection limit $V = 23.5$. For sources with multiple counterparts, the range on $\log(F_X/F_V)_u$ is indicated with a vertical line. Error bars on the flux ratio only include statistical errors, not any systematic errors resulting from uncertainties in the adopted X-ray spectral model. CX 150 is an outlier and may be spuriously matched to the star in its error circle. Only sources with $\sigma_{E_{50}} < 1$ are plotted.

but with errors on E_{50} that are too large ($\gtrsim 1$ keV) to meaningfully constrain their X-ray spectra; these sources were classified as "AB?". CX 25 is an uncertain AB because its position in the quantile diagram suggests an N_H that is enhanced with respect to the Galactic column, which is not expected for typical ABs. Finally, CX 41 and CX 57 have $E_{50} = 2.2 \pm 0.5$ keV and 2.5 ± 0.5 keV, respectively; this is on the high side for ABs, but given the large errors, we also put these two sources in the "AB?" category. With $B - V = 1.34$ at $V = 20.15$, CX 41 is relatively blue, but not as offset from the main sequence as the sources discussed in Sect. 4.2; however, it is not inconceivable that this source is an AGN or a CV. We expect that a significant number of "AB" and "AB?" sources are fore- and background active stars or binaries.

Ten ABs are matched to Mazur variables. CX 27/V42, CX 89/V11, CX 97/V38, and CX 138/V21 are (semi-)detached eclipsing binaries. The first three have periods of 1.3 d or shorter, while the light curve of V21 shows eclipse-like events with an unconstrained period. The maximum orbital period that can be tidally circularised in ~7 Gyr (i.e. the age Cr 261) is ~15 d (Mathieu et al. 2004). Since the time scale for tidal synchronisation is shorter than that for circularisation (Hut 1981; Zahn 1989), it is perfectly plausible that at least V42, V11, and V38 contain rapidly rotating, and therefore X-ray–active, stars. CX 93/V30, CX 126/V13, CX 133/V10[8], CX 144/V24, CX 147/V25, and CX 149/V33

[8] CX 133 is matched with two stars on the main sequence; V10 is the more likely counterpart of the two.

are contact binaries of the W UMa type. For W UMa's, a distance constraint can be derived from the known calibration of the absolute magnitudes in terms of orbital period and $B-V$ or $V-I$ colour (see e.g. Rucinski & Duerbeck 1997). Mazur et al. thus found that the distances to V30, V13, V25, V33, and likely V24, are compatible with that of Cr 261; these are the most reliable cluster ABs in our sample. Mazur et al. were inconclusive regarding the distance to V10.

The time span of the WFI observations is ~0.75 h, with the B data taken first. For CX 149/V33, with a period of 6.96 h and a large-amplitude (~0.8 mag) light curve, this spans ~0.1 in orbital phase. If our observations happened to be timed around eclipse ingress (something we cannot check because the ephemeris is not known with sufficient precision), this can explain why we find a much bluer colour ($B-V=0.72$) than Mazur et al., who report $B-V=1.09$, i.e. right on the main sequence. We found similar colour differences for a few other variables. Mazur et al. adopted a method that makes their colours much less sensitive to non-simultaneous measurements. Therefore, in Figure 3, we plotted the variables with their Mazur photometry (see Table 3), if available.

4.2. *Candidate Cataclysmic Variables or AGN*

Our mass estimate for Cr 261 (5800–7200 $M_\odot$) is similar to the mass of NGC 6791 (5000–7000 $M_\odot$). If CVs in open clusters are primordial, Cr 261 would host a similar number of CVs as NGC 6791, i.e. 3 to 4 (van den Berg 2013). CVs typically lie to the blue of the main sequence due to the light from the accretion disk, and possibly from the white dwarf (although in the B band, the blue excess is not always that obvious, see e.g. Bassa et al. 2008). For eleven sources, the candidate optical counterpart(s) are blue with respect to the main sequence, and ten of them are possibly CVs: CX 4, CX 8, CX 20, CX 22, CX 24, CX 38, CX 44, CX 54, CX 70, and CX 151[9]. The other blue source, CX 120, is not a member of the cluster (see Sect. 4.4). We consider a source to be blue if it lies to the left of the isochrone that is reddened for the lowest possible cluster reddening. In addition, we require the blueward offset from this isochrone to be at least 0.13 mag, i.e. the errors on the absolute photometric calibration in V and B added in quadrature (see Sect. 3.2).

The ten sources listed above have E_{50} values between ~1.5 and 2.8 keV, $\log(F_X/F_V)_u$ between –2.5 and +1.0, and L_X between 5×10^{29} and 3×10^{31} erg s^{-1}. This is consistent with a CV classification, although $\log(F_X/F_V)_u \approx -2.5$ for CX 151 is on the low side for a CV; this may suggest a different source class or the presence of a random interloper in the X-ray error circle. We label these sources as candidate CVs ("CV?" in Table 2). Confusion with other classes in this part of the CMD is mainly with AGNs, which outnumber the CVs in the field observed (Sect. 3.5) and can have similar blue colours and X-ray properties. However, since very few CVs in open clusters have been found, it is worthwhile to highlight any candidates. Follow-up optical spectroscopy can confirm or disprove whether a source is a CV nor not.

[9] The optical match to CX 22, and one of the matches to CX 24, are only detected in B, but the detection limit in V implies they must be blue ($B-V\lesssim0.7$).

4.3. *Candidate Blue Stragglers, Yellow Stragglers, and Sub-subgiants*

Some of the brightest X-ray sources in old open clusters are members that lie off the main locus of the cluster in the CMD. These systems challenge our understanding of binary evolution, and, in some cases, we do not understand why they emit X-rays (van den Berg et al. 1999). Therefore, they deserve special attention.

Blue straggler stars (BSSs) are bluer and brighter than the main-sequence turnoff (MSTO) of a coeval population. Their formation scenarios must explain how these stars managed to continue core hydrogen burning for a longer time than cluster stars of similar mass. Mass transfer in a binary, direct collisions, and the merger of the close inner binary in a hierarchical triple driven by the Kozai-Lidov mechanism, are the three proposed formation channels (Davies 2015). For most BSSs, it is not clear which (if any) of these channels applies. The detection of X-rays in a bona-fide cluster BSS is a sign of ongoing binary interaction and thus provides a clue to the current system configuration. There is no strict brightness limit with respect to the MSTO that we can use to select candidate BSSs in Cr 261. In M 67, which has one of the best-studied BSSs populations, the brightest BSS (F 81; Leonard 1996) lies ~2.7 mag above the MSTO in the V band. We take the equivalent location in the CMD of Cr 261, i.e. $V\approx14$, as a (somewhat arbitrary) limit, and consider brighter stars to be non-members. We thus find eight matches with candidate BSSs: CX 18/V45, CX 67, CX 73, CX 74, CX 86/V12, CX 130, CX 132, and CX 136/V22. Except for CX 67, these sources are soft ($E_{50}\lesssim1.4$ keV) and all have $\log(F_X/F_V)_u$ between –3.9 and –2.8. This is consistent with the properties of ABs, and their X-rays are therefore likely the result of magnetic activity. Indeed, three sources are matched to (semi-)detached eclipsing binaries with periods between 1.1 and 2.1 d. V12 and V22 show Algol-type light curves. The idea of a possible link between Algols and BSSs was already put forth by McCrea (1964). In an Algol binary, the originally less massive star is now observed to be the more massive one as a result of the mass it received from its Roche-lobe filling companion—here we may be seeing a BSS "in the making". It would therefore be particularly interesting to determine if V12 and V22 are cluster members.

The candidate counterparts of CX 9 and CX 123 lie between the BSSs and red giants. Stars in this region of the CMD have been dubbed yellow stragglers and may be BSS descendants. All yellow stragglers in M 67 are solid cluster members and X-ray sources (Belloni et al. 1998). Their X-ray properties point at the presence of magnetic activity, and the same appears to be the case for CX 9 and CX 123.

Finally, sub-subgiants (SSGs) or red stragglers, lie below the sub-giant branch or to the red of the base of the giant branch. Whereas BSSs seem to have somehow managed to prolong their main-sequence lifetime, SSGs resemble (sub-)giants that have evolved from stars less massive than the turnoff mass. Little is known about the evolutionary history that has led to their current CMD position (see van den Berg (2013) for a summary). We see three candidate SSGs in Cr 261: CX 12, CX 31, and perhaps CX 58. Their X-ray properties are consistent with those of ABs. CX 58 may be too faint for a SSGs, but just as there is no "bright" limit for BSSs, there is no well-defined "faint" limit for SSGs.

The alternative explanation for the sources discussed above is that they are foreground stars. Assuming $N_H = 0$, they could be early-G to late-K foreground dwarfs at distances up to 1.6 kpc (Mamajek 2016[10]) with $L_X \approx (4-9)\times10^{27}$ erg s^{-1}.

4.4. *Cluster Non-members*

CX 120 and CX 68 are matched to the variables V34 and V20, respectively. V34 was classified as a W UMa binary behind the cluster. The eclipsing binary V20 lies well to the red of the main sequence, which makes it an unlikely cluster member. Their X-ray properties are consistent with those of ABs. Six more X-ray sources have very red counterparts: CX 10, CX 15, CX 53, CX 77, CX 91, and CX 137. If we assume these are foreground ($N_H \approx 0$) late-type stars, their $B-V$ colours suggest they are mid- to late-type M dwarfs at about 40–215 pc; this implies $L_X \approx 1\times10^{26}$ to 4×10^{28} erg s^{-1}. CX 91 and CX 137 are variable in X-rays, which could point at flares, another signature of coronal activity. The position in the quantile diagram of CX 15 suggests an N_H that is higher than the cluster value; it could be an AGN. For CX 10 and CX 77, E_{50} is relatively high and they as well may be AGNs.

The soft ($E_{50} \lesssim 1.4$ keV) sources CX 7, CX 30, CX 40, CX 59, CX 95, CX 100 and CX 129 have counterparts that are brighter ($V = 11.4-13.7$) than our adopted bright limit for blue stragglers in the cluster. These are likely foreground stars. We also consider CX 55, which is matched to a star to the blue of the MSTO, as a likely non-member. Their $B-V$ colours are consistent with those of mid-F to mid-K dwarfs (for $N_H = 0$). Using the corresponding distance estimates (75–2400 pc), we find $L_X \approx (0.1-20)\times10^{29}$ erg s^{-1}.

4.5. *Unclassified Sources*

Nineteen sources remain unclassified for various reasons. Six have candidate counterparts that were only detected in V, so colour information is lacking. Eleven sources have multiple counterparts with very different optical properties, including some that were detected in V or B only. CX 14 is a moderately hard source matched to two optical sources near the main sequence. Its N_H appears to be higher than the Galactic value (Figure 2); it may be an AGN and both optical matches could be spurious. Finally, CX 150 is one of the faintest detections; if the source is real, E_{50} suggests it is a very hard, or very absorbed, source (Figure 5). The match to the star on the sub-giant branch may be coincidental.

[10] http://www.pas.rochester.edu/~emamajek/EEM_dwarf_UBVIJHK_colors_Teff.txt

4.6. *Sources Without Candidate Optical Counterparts*

For 53 sources, we do not find any candidate optical counterparts. With the detection limit of the WFI images ($V \approx 23.5$), we can place lower limits on their X-ray–to–optical flux ratios. These range from $\log(F_X/F_V)_{u,lim} \approx -0.6$ for the faintest (CX 146) to $\log(F_X/F_V)_{u,lim} \approx 1.5$ for the brightest (CX 1) unmatched source. This is consistent with very active late-type dwarfs and accretion-powered sources. The average E_{50} for unmatched sources is 2.1 ± 0.5 keV, versus 1.7 ± 0.6 keV for sources that do have candidate counterparts (for detections with 10 or more counts). Given that we expect many extra-galactic sources in our field (see Sect. 3.5), it is likely that most sources without an optical match are AGNs.

5. DISCUSSION

5.1. *Comparison with Other Old Open Clusters*

In order to uniformly compare our results with the X-ray sources in other old open clusters, we select those sources from the Cr 261 X-ray catalogue that are inside r_h, and are brighter than $L_X \approx 1\times10^{30}$ erg s^{-1} (for cluster members). For a detection limit of $L_X \approx 1\times10^{30}$ erg s^{-1} (0.3 –7 keV; 2 keV MeKaL model), about 57±8 of the 83 sources inside r_h above this luminosity cutoff are extra-galactic. Consequently, we estimate that 26±8 sources in this area are associated with the cluster, and consider this an upper limit given the uncertain number of fore- and background Galactic sources.

Allowing for the limitations on our classification, we list in Table 4 our best estimate for the number of candidate CVs, SSGs, and ABs in Cr 261 (based on the discussion in Sect. 4), and three other old open clusters. The lower limit on N_{AB} in Cr 261 is set by the two W UMa's inside r_h that Mazur et al. (1995) place at the distance of Cr 261, viz. CX 93/V30 and CX 147/V25. Note that these classes do not capture all source types observed, since some are not represented in each cluster (such as BSSs). In the table we also list a revised mass estimate for M 67. Instead of ~1100 $M_\odot$ (Richer et al. 1998) that we adopted in van den Berg et al. (2013), we now use the virial mass of 2100^{+610}_{-550} $M_\odot$ (Geller et al. 2015). Within the uncertainty, the total number of X-ray sources N_X in Cr 261 is consistent with the number for NGC 6791, a cluster of similar mass and age. Considering all four clusters, N_X scales with mass more convincingly than before (van den Berg et al. 2013), now that we add a fourth cluster (Cr 261) and use the updated mass for M 67—but N_{AB} in M 67 remains on the high side. A scaling by mass is expected if the X-ray sources predominantly trace a primordial population of binaries. Since ABs are the largest constituent of the X-ray sources, all or most of them are likely primordial, but whether this is also

true for all CVs and SSGs is difficult to say given the small-number statistics.

By combining our mass estimate with the total X-ray luminosity of cluster sources inside r_h, we compute the X-ray emissivity of Cr 261 (last column of Table 4). We do not know which sources inside r_h are cluster members and which are not. Therefore, we simply scale down the sum of the individual L_X values by the ratio of N_X to the total number of sources detected, so a factor $26/83 \approx 0.31$. Given the uncertainty in the membership, a more sophisticated calculation is not really warranted. For NGC 6791, the emissivity was taken from van den Berg et al. (2013), and for M 67 we updated the value for the new mass. We incorporated new counterpart and membership information from Platais et al. (2013) in the numbers for NGC 6819; the range in emissivity reflects more and less conservative assumptions on which counterparts are cluster members or not. The conversion of the X-ray luminosities from the 0.2–10 keV band, as given in Gosnell et al. (2012), to our adopted band of 0.3–7 keV was done assuming a 2 keV MeKaL model. Uncertainties in the emissivities are likely dominated by errors in the cluster masses (up to ~30% for M 67) and the unknown membership status of some sources, especially if they are bright. Systematic uncertainties in the X-ray luminosities themselves have less impact: in Sect. 3.1 we estimated that the difference in flux for a 1 keV and 2 keV X-ray model is ~6%; given that most X-ray sources are ABs, with coronal temperatures not too far from these values, it is not likely that the choice of X-ray model affects the total X-ray flux by more than ~10%. Allowing for these uncertainties, the four open clusters listed in Table 4 all have similar X-ray emissivities, about 5×10^{28} erg s^{-1} $M_\odot^{-1}$ (0.3–7 keV).

5.2. *Comparison with Other Old Stellar Populations*

It has already been pointed that extrapolating the scaling relation of the number of X-ray sources by mass as seen in low-density globular clusters, predicts no X-ray emitting close binaries in the even lower-density open clusters (see e.g. Gosnell et al. 2012) like those listed in Table 4. This is clearly in contrast with the number of open-cluster X-ray sources actually observed. Our results on Cr 261 are in line with this trend; by adding another measurement to the cluster sample, the perceived "overabundance" of X-ray sources in open clusters is put on more solid ground.

The dearth of ABs and CVs is directly reflected in the lower X-ray emissivity of both low-density and high-density globular clusters compared to old open clusters (Verbunt 2001; Huang et al. 2010; van den Berg et al. 2013; Ge et al. 2015). Even the emission from quiescent LMXBs and millisecond pulsars, whose presence has so far only been confirmed in globular clusters, cannot make up for that. Some suggested explanations for the differences in X-ray emissivity relate to dynamical processes. A higher fraction of the initial cluster mass may have been lost (in the form of evaporating low-mass stars) from open clusters, as their relaxation times are shorter than those of more massive globular clusters. Also, the higher encounter rates in massive globular clusters lead to the more efficient destruction of binaries, including (relatively wide) RS CVn binaries that contribute a large fraction of the X-rays from (some) open clusters. Other possible explanations relate to the process that underlies the X-ray emission. Huang et al. (2010) remarked that open clusters are younger than globulars, and that the faster-spinning young stars could be more active in X-rays (here we note that the stellar rotation in binaries is set by the orbital period, not the age). In addition, open clusters have higher metallicities than globular clusters, and there are indications that population-I ABs produce more X-rays than their population-II counterparts (Ottmann et al. 1997).

Interestingly, in a broader comparison of X-ray emissivities of old stellar populations, Ge et al. (2015) found that old open clusters not only have higher X-ray emissivities than globular clusters, but also than other old stellar populations without recent star formation, such as dwarf ellipticals, the outer bulge of M 31, and the solar neighbourhood. In those environments, the stellar density is much lower than in the cores of massive globular clusters, casting doubt on whether differences in density are solely responsible for the difference in X-ray output of old stellar populations.

6. SUMMARY

With *Chandra* we have carried out the first X-ray study of Cr 261, one of the oldest open clusters known in the Galaxy. We detected 151 X-ray sources down to a limiting luminosity of $L_X \approx 4 \times 10^{29}$ erg s^{-1} (0.3–7 keV) for stars in the cluster. Analysis of deep optical B and V images yielded candidate counterparts to 98 sources. Considering their X-ray and optical properties, we were able to derive constraints on the nature of many sources, despite the lack of membership information. Of the 107 sources inside r_h, five are CVs (or other compact binaries) or AGNs. Another 34 sources are (candidate) ABs, and eleven match with stars that possibly followed non-standard evolutionary paths in the cluster environment (blue and yellow stragglers, sub-subgiants)—this group is likely contaminated by fore- and background stars. The remaining sources inside r_h have no optical counterparts (39), have ambiguous classifications (7), or match with stars that are very bright or very red (11); we expect that most of these are not associated with the cluster. Follow-up work on the Cr 261 sources, such as optical spectroscopy of the proposed counterparts, or proper-motion studies, are now needed to further constrain the nature and membership status of the X-ray sources in Cr 261, and arrive at a cleaner census of the close binaries.

We used our optical source catalogue to derive an approximate mass for Cr 261. The total number of X-ray sources inside r_h above $L_X = 1 \times 10^{30}$ erg s^{-1} (corrected for the extragalactic background contribution) compared to the number of X-ray sources in other old open clusters, is roughly propor-

tional with cluster mass. This points at a dominant primordial origin of the X-ray–emitting sources. Combining the mass with the total X-ray luminosity of cluster sources, we have constrained the X-ray emissivity of Cr 261. The result, $\sim 5{\times}10^{28}$ erg s^{-1} $M_{\odot}^{-1}$ (∼30% uncertainty), agrees with that of the old open clusters NGC 6819, M 67, and NGC 6791. This supports earlier findings that old open clusters are more luminous in X-rays than other old stellar populations, such as the local neighbourhood and globular clusters. Given that the frequency of dynamic encounters in globular clusters and the field is widely different, one may expect that dynamical destruction of binaries is not (solely) responsible for the relatively suppressed X-rays from these environments. It is plausible that the explanation for the high X-ray emissivity of old open clusters must be sought in the open clusters themselves. Other old open clusters included in our *Chandra* survey span a range of ages (3.5–10 Gyr) and metallicities ([Fe/H] between –0.5 and +0.4); our future work will explore the impact of these parameters on the X-ray emission of old stellar clusters.

The authors would like to thank J. Hong for help with the computation of the energy quantiles, L. Bedin for doing a quick-look reduction of the optical WFI data, and R. Wijnands for comments on an early version of the manuscript. We are grateful to A. Bragaglia for sharing an optical catalog of Cr 261 stars to aid in the photometric calibration. Part of this work is based on observations made with ESO Telescopes at the La Silla Paranal Observatory under programme ID 164.O-0561. This work is supported by *Chandra* grant GO0-11110X. S.V. acknowledges the support of NOVA (Nederlandse Onderzoekschool voor Astronomie)

Facilities:

Facility: CXO

Facility: Max Planck:2.2m (WFI)

Table 1. Catalogue of *Chandra* sources in Cr 261

(1) CX	(2) CXOU J	(3) α (J2000.0) (°)	(4) δ (J2000.0) (°)	(5) Error (″)	(6) θ (′)	(7) $C_{t,net}$	(8) $C_{s,net}$	(9) $F_{X,u}$ (10^{-15} erg cm^{-2} s^{-1})	(10) E_{50} (keV)	(11) Optical Match
1	123823.4-682206	189.597301	–68.368591	0.31	2.07	473±22	226±15	100	2.1±0.1	–
2	123740.9-682730	189.420561	–68.458567	0.55	4.64	139±12	74±9	31	1.8±0.2	–
3	123854.1-681556	189.725375	–68.265715	0.86	8.75	121±12	38±6	31	2.7±0.19	–
4	123902.9-682228	189.761982	–68.374587	0.53	5.35	116±11	70±8	29	1.74±0.09	+
5	123932.0-682559	189.883288	–68.433159	1.06	8.18	101±10	17±4	27	3.19±0.17	–
6	123750.6-682807	189.460702	–68.468808	0.63	4.83	94±10	32±6	21	2.6±0.3	–
7	123832.5-682949	189.635595	–68.497007	0.92	6.70	93±10	90±10	24	1.10±0.06	+
8	123839.7-681726	189.665606	–68.290676	0.64	6.80	89±10	53±7	19	1.74±0.13	+
9	123759.1-681609	189.496354	–68.269261	0.76	7.42	71±9	52±7	16	1.29±0.07	+
10	123744.9-682032	189.437242	–68.342330	0.41	3.63	63±8	32±6	13	2.0±0.3	+
11	123734.7-681418	189.394755	–68.238507	1.35	9.70	61±8	29±6	17	2.1±0.4	–
12	123751.3-682535	189.463891	–68.426524	0.46	2.51	61±8	54±7	14	1.18±0.07	+
13	123757.7-682421	189.490520	–68.406048	0.39	1.19	52±7	46±7	10	1.21±0.08	+
14	123953.6-682051	189.973426	–68.347770	2.03	10.18	50±8	23±5	12	2.3±0.4	+
15	123931.8-681730	189.882528	–68.291885	1.73	9.87	49±8	11±4	14	2.8±0.3	+
16	123923.5-682200	189.848009	–68.366711	1.06	7.21	45±7	24±5	11	1.8±0.5	–
17	123821.7-682820	189.590529	–68.472426	0.84	4.99	44±7	13±4	11	3.0±0.4	+
18	123816.6-682518	189.568966	–68.421935	0.46	1.98	41±6	32±6	9.1	1.32±0.11	+
19	123817.2-682039	189.571664	–68.344429	0.40	3.02	41±6	30±5	8.2	1.50±0.12	–
20	123821.3-681312	189.588903	–68.220081	1.99	10.42	40±7	27±6	10	1.55±0.15	+
21	123758.7-683058	189.494717	–68.516135	1.68	7.47	38±7	20±5	9.5	2.0±0.5	–
22	123842.1-681326	189.675256	–68.224149	2.32	10.60	34±7	17±5	9.8	2.1±0.4	+
23	123704.7-682331	189.269643	–68.392221	0.97	5.74	28±6	4±2	6.9	3.4±0.3	–
24	123939.5-681858	189.914529	–68.316227	2.38	9.67	28±6	16±4	7.0	1.7±0.4	+
25	123918.7-681611	189.827710	–68.269811	2.32	9.89	28±6	23±5	12	1.48±0.12	+
26	123707.4-682334	189.280972	–68.392931	0.96	5.49	26±5	11±4	6.0	2.6±0.7	–
27	123850.3-681639	189.709667	–68.277553	1.44	7.96	25±5	21±5	6.0	1.15±0.18	+
28	123716.3-682518	189.318042	–68.421875	0.94	4.99	24±5	20±5	5.6	1.06±0.13	+
29	123753.5-682000	189.472784	–68.333349	0.50	3.76	24±5	17±4	6.8	1.51±0.17	+
30	123836.9-682721	189.653872	–68.455995	0.99	4.70	24±5	23±5	5.0	1.4±0.2	+
31	123823.4-682820	189.597668	–68.472407	1.13	5.03	24±5	18±4	6.1	1.40±0.14	+
32	123716.3-682036	189.317855	–68.343371	0.86	5.53	23±5	16±4	5.0	1.3±0.2	–
33	123804.7-682334	189.519709	–68.392814	0.40	0.22	23±5	12±4	4.6	1.9±0.4	–
34	123858.4-681743	189.743326	–68.295490	1.39	7.50	22±5	10±3	5.9	2.1±0.4	–
35	123732.9-682648	189.386958	–68.446727	0.96	4.53	22±5	15±4	5.0	1.94±0.15	–
36	123656.3-682204	189.234675	–68.367933	1.35	6.68	22±5	12±4	7.9	1.9±0.4	+
37	123914.6-682316	189.810739	–68.387795	1.30	6.22	20±5	12±4	4.5	1.9±0.5	–
38†	123735.9-681430	189.399430	–68.241885	2.47	9.48	20±5	12±4	6.1	1.8±0.2	+
39	123805.6-682623	189.523310	–68.439846	0.69	2.85	20±4	9±3	4.0	2.6±0.5	–
40	123715.7-682728	189.315302	–68.457948	1.61	6.15	19±5	17±4	7.6	1.23±0.11	+
41	123707.5-682443	189.281093	–68.412219	1.22	5.61	19±5	8±3	4.3	2.5±0.5	+
42	123846.8-682650	189.695026	–68.447337	1.14	4.92	19±5	6±3	4.0	2.8±0.6	–

continued on next page

(1) CX	(2) CXOU J	(3) α (J2000.0) (°)	(4) δ (J2000.0) (°)	(5) Error (″)	(6) θ (′)	(7) $C_{t,net}$	(8) $C_{s,net}$	(9) $F_{X,u}$ (10^{-15} erg cm^{-2} s^{-1})	(10) E_{50} (keV)	(11) Optical Match
43	123709.4-682708	189.289121	–68.452257	1.77	6.41	18±5	4±2	4.9	2.5±0.5	–
44†	123640.6-682122	189.169352	–68.356137	2.39	8.25	18±5	8±3	4.4	2.8±0.9	+
45	123711.6-682036	189.298332	–68.343498	1.10	5.89	18±4	7±3	3.8	2.1±0.7	–
46	123835.2-683046	189.646754	–68.512900	2.90	7.68	18±5	12±4	4.2	1.2±0.5	+
47	123751.1-682620	189.463038	–68.438966	0.77	3.16	17±4	10±3	4.0	1.9±0.6	+
48	123729.2-681706	189.371654	–68.285207	1.49	7.32	17±4	12±4	4.7	1.6±0.4	–
49	123725.4-682443	189.355865	–68.412196	0.86	4.01	16±4	15±4	3.5	1.26±0.20	+
50	123808.9-681613	189.537120	–68.270460	1.4	7.32	16±4	9±3	3.7	1.8±0.7	–
51	123759.1-682510	189.496064	–68.419466	0.56	1.79	16±4	12±4	3.6	1.3±0.3	+
52	123645.0-681926	189.187449	–68.324003	2.73	8.61	16±5	7±3	3.7	2.2±0.6	–
53	123835.4-681447	189.647524	–68.246512	2.69	9.13	15±5	10±4	4.1	1.8±0.8	+
54	123810.7-682750	189.544666	–68.464116	1.19	4.32	15±4	7±3	3.8	2.3±0.5	+
55†	123928.7-682454	189.869435	–68.415071	2.58	7.63	15±5	7±3	3.4	1±2	+
56	123741.3-682130	189.422082	–68.358334	0.55	3.13	15±4	9±3	3.4	1.6±0.4	–
57†	123913.9-681834	189.807786	–68.309638	2.15	7.91	15±4	7±3	3.7	2.2±0.5	+
58	123912.6-682737	189.802665	–68.460385	2.64	7.28	15±5	15±4	3.5	1.4±0.1	+
59	123752.8-682559	189.469961	–68.433066	0.74	2.77	15±4	15±4	3.8	0.95±0.06	+
60	123656.6-682452	189.235923	–68.414656	1.98	6.62	14±4	7±3	3.7	2.4±0.7	–
61	123800.5-682710	189.502237	–68.452840	1.00	3.68	14±4	7±3	3.3	2.3±0.8	+
62†	123911.1-681705	189.796169	–68.284874	2.76	8.75	14±5	5±3	3.4	2±1	+
63†	123926.8-682508	189.861487	–68.418971	2.66	7.50	14±4	12±4	3.4	1.2±0.2	+
64	123708.8-682321	189.286700	–68.389211	1.27	5.37	14±4	11±3	3.0	1.3±0.3	+
65	123802.7-683000	189.511184	–68.500163	2.50	6.48	14±4	7±3	3.2	1.8±0.9	+
66†	123724.4-682854	189.351711	–68.481709	2.53	6.64	13±4	8±3	3.6	2±1	–
67	123908.7-682405	189.786450	–68.401525	1.51	5.70	13±4	8±3	3.1	1.9±0.3	+
68	123732.9-682254	189.387088	–68.381922	0.67	3.21	13±4	9±3	2.7	1.0±0.3	+
69†	123933.4-681758	189.889151	–68.299714	4.41	9.71	12±5	5±3	3.1	2±1	+
70	123758.4-682301	189.493504	–68.383764	0.44	0.95	12±4	9±3	3.7	1.6±0.3	+
71	123819.9-681908	189.582922	–68.319011	0.76	4.56	12±4	7±3	2.4	1.8±0.8	–
72	123858.3-682703	189.742924	–68.450945	2.07	5.88	11±4	4±2	2.5	2.1±0.4	–
73	123859.9-682307	189.749388	–68.385393	1.18	4.88	11±4	11±3	2.3	1.05±0.18	+
74	123744.2-682828	189.434117	–68.474621	1.95	5.36	11±4	11±4	2.6	1.1±0.3	+
75	123833.4-681621	189.639295	–68.272733	2.08	7.58	11±4	7±3	2.6	1.6±0.9	–
76	123839.4-682609	189.664144	–68.436102	1.14	3.97	11±4	5±2	2.3	2.4±0.5	–
77†	123920.3-681804	189.834519	–68.301311	3.40	8.69	11±4	4±2	2.6	2.7±0.9	+
78	123759.8-682303	189.499214	–68.384224	0.45	0.83	11±3	6±3	6.0	2.0±0.4	+
79	123755.2-682514	189.479947	–68.420605	0.67	2.02	11±3	7±3	2.3	1.5±0.4	–
80†	123723.4-682745	189.347313	–68.462565	2.21	5.82	11±4	6±3	2.6	2±1	+
81	123809.9-682032	189.541149	–68.342477	0.53	3.00	11±3	10±3	2.5	1.2±0.2	+
82	123811.7-682522	189.548553	–68.423049	0.67	1.89	11±3	9±3	2.2	1.5±0.2	+
83†	123755.0-681542	189.479307	–68.261917	2.39	7.91	11±4	2±2	2.7	3.3±0.5	+
84	123813.6-682637	189.556813	–68.443847	0.99	3.15	10±3	3±2	2.2	2.1±0.6	–

continued on next page

(1) CX	(2) CXOU J	(3) α (J2000.0) (°)	(4) δ (J2000.0) (°)	(5) Error (″)	(6) θ (′)	(7) $C_{t,net}$	(8) $C_{s,net}$	(9) $F_{X,u}$ (10^{-15} erg cm^{-2} s^{-1})	(10) E_{50} (keV)	(11) Optical Match
85	123815.4-682427	189.564219	–68.407599	0.57	1.19	10±3	7±3	2.0	1.2±0.5	+
86	123816.7-682436	189.569630	–68.410056	0.59	1.38	10±3	6±3	2.0	1.4±0.7	+
87	123828.2-682116	189.617623	–68.354598	0.58	2.99	10±3	8±3	2.0	1.3±0.3	+
88	123823.4-681706	189.597632	–68.285277	1.63	6.60	10±3	10±3	2.2	1.03±0.16	+
89	123757.3-682502	189.488645	–68.417264	0.68	1.75	9±3	7±3	2.1	1.1±0.4	+
90	123818.0-682417	189.574953	–68.404962	0.58	1.26	9±3	6±3	1.8	1.5±0.5	–
91†	123844.8-682606	189.686473	–68.435269	1.44	4.32	9±3	6±3	1.8	1.3±0.9	+
92	123630.8-682249	189.128208	–68.380359	5.51	8.90	9±4	9±4	2.6	1.39±0.15	+
93	123731.1-682128	189.379664	–68.357778	0.86	3.91	9±3	5±2	1.9	1±1	+
94	123800.6-682159	189.502590	–68.366532	0.47	1.66	9±3	9±3	1.8	0.99±0.10	+
95	123832.8-682202	189.636665	–68.367275	0.63	2.81	9±3	9±3	1.7	1.12±0.16	+
96†	123918.9-682558	189.828694	–68.432881	3.44	7.04	9±4	2±2	2.2	2.6±0.3	+
97†	123812.1-681712	189.550429	–68.286827	1.60	6.35	9±3	8±3	2.0	1.13±0.18	+
98	123828.0-682442	189.616733	–68.411870	0.74	2.25	9±3	6±2	1.8	1.4±0.7	–
99	123755.7-682607	189.482014	–68.435438	0.97	2.79	9±3	6±2	2.1	1.5±0.6	–
100	123835.4-682622	189.647542	–68.439534	1.36	3.85	8±3	9±3	1.7	0.93±0.08	–
101	123839.9-682811	189.666443	–68.469832	2.61	5.54	8±3	5±2	1.7	1.1±0.7	–
102	123810.6-682104	189.544130	–68.351119	0.53	2.50	8±3	2±2	1.8	2.9±0.5	–
103	123823.8-682330	189.599256	–68.391940	0.58	1.54	8±3	5±2	1.5	1.7±0.7	+
104†	123833.7-682011	189.640396	–68.336559	0.88	4.15	8±3	4±2	1.7	2.0±0.4	–
105	123841.7-682104	189.673821	–68.351302	0.92	4.03	8±3	7±3	1.6	1.5±0.2	–
106	123836.8-682013	189.653477	–68.337185	0.94	4.30	8±3	5±2	1.7	1.8±0.3	–
107	123839.3-682014	189.663567	–68.337314	1.00	4.44	8±3	2±2	1.7	2.7±0.8	–
108†	123806.6-682616	189.527489	–68.437998	1.05	2.74	8±3	3±2	1.6	3.3±0.8	–
109†	123811.4-681308	189.547534	–68.219135	7.78	10.40	7±4	<2.5	2.1	5±1	+
110	123815.9-682134	189.566252	–68.359664	0.53	2.12	7±3	2±2	3.8	2.2±0.8	–
111	123738.9-682118	189.412214	–68.355234	0.80	3.42	7±3	<1.1	1.6	4.8±0.5	–
112	123800.2-682511	189.500897	–68.419799	0.78	1.76	7±3	3±2	1.6	2.1±0.7	+
113	123745.9-682109	189.441337	–68.352636	0.69	3.08	7±3	3±2	1.8	2.1±0.8	–
114	123826.9-681859	189.611891	–68.316430	1.16	4.91	7±3	6±3	1.5	1.1±0.4	+
115	123826.1-682534	189.608694	–68.426193	1.04	2.68	6±3	5±2	1.3	1±1	+
116	123841.3-682447	189.672185	–68.413140	1.19	3.39	6±3	4±2	1.3	2±1	–
117†	123718.3-681822	189.326262	–68.306383	2.86	6.84	6±3	2±2	1.3	3±2	–
118	123812.7-682301	189.552882	–68.383798	0.53	0.73	6±3	2±2	1.2	3.0±0.9	–
119†	123714.9-682018	189.311995	–68.338503	2.18	5.80	6±3	7±3	1.3	0.9±0.2	+
120†	123829.0-681920	189.620718	–68.322330	1.25	4.66	5±2	5±2	1.1	1.2±1.1	+
121†	123809.3-681438	189.538731	–68.244009	6.38	8.90	5±3	6±3	1.2	1.05±0.06	+
122	123832.6-682324	189.635758	–68.390217	0.85	2.35	5±2	0.	2.2	3.7±0.6	–
123	123759.7-682349	189.498816	–68.397053	0.65	0.73	5±2	3±2	1.0	1±1	+
124	123805.9-682255	189.524767	–68.382160	0.56	0.62	5±2	4±2	0.97	1.1±0.4	+
125	123808.4-681937	189.535049	–68.327083	0.95	3.92	5±2	4±2	0.99	1±1	+
126	123811.6-682410	189.548339	–68.402850	0.69	0.75	5±2	5±2	0.97	1.2±0.3	+

continued on next page

(1) CX	(2) CXOU J	(3) α (J2000.0) (°)	(4) δ (J2000.0) (°)	(5) Error (″)	(6) θ (′)	(7) $C_{t,net}$	(8) $C_{s,net}$	(9) $F_{X,u}$ (10^{-15} erg cm^{-2} s^{-1})	(10) E_{50} (keV)	(11) Optical Match
127†	123919.1-682346	189.829698	–68.396355	4.42	6.64	5±3	6±3	1.3	1.0±0.2	+
128†	123727.2-682316	189.363451	–68.387783	1.36	3.68	5±2	5±2	1.1	0.9±0.3	+
129	123743.7-682518	189.432199	–68.421940	1.26	2.79	5±2	5±2	1.1	1.2±0.2	+
130	123814.3-682002	189.559538	–68.334078	0.86	3.56	5±2	5±2	0.97	0.89±0.13	+
131†	123646.3-682528	189.192806	–68.424563	7.43	7.68	5±3	<1.1	1.3	5.9±0.7	+
132	123845.3-682336	189.688697	–68.393346	1.34	3.52	5±2	5±2	1.1	0.87±0.10	+
133†	123744.6-682543	189.436025	–68.428709	1.45	3.00	5±2	5±2	1.2	1.6±0.2	+
134	123822.2-682557	189.592308	–68.432742	1.39	2.79	5±2	5±2	0.95	0.9±0.2	+
135†	123731.0-681841	189.379262	–68.311663	2.37	5.87	4±2	4±2	1.8	1.7±0.8	+
136	123751.4-682234	189.464318	–68.376236	0.72	1.74	4±2	4±2	0.94	1.09±0.13	+
137	123758.9-682407	189.495337	–68.402109	0.79	0.95	4±2	4±2	0.80	1.58±0.18	+
138†	123800.1-682234	189.500230	–68.376235	0.63	1.16	4±2	3±2	1.1	1.5±0.4	+
139†	123805.5-682100	189.523107	–68.350180	0.72	2.53	4±2	4±2	1.1	1.22±0.18	+
140†	123812.4-682441	189.551614	–68.411460	0.90	1.25	4±2	2±2	0.86	2±1	–
141†	123735.4-682040	189.397562	–68.344524	1.39	4.09	4±2	<1.1	0.94	4±1	–
142	123805.2-682531	189.521504	–68.425483	1.21	1.99	4±2	4±2	0.89	1.5±0.3	+
143	123806.8-681914	189.528172	–68.320569	1.29	4.31	4±2	4±2	0.77	0.9±0.3	+
144†	123842.4-682204	189.676583	–68.367882	1.33	3.57	4±2	4±2	0.79	0.7±0.3	+
145†	123828.5-682624	189.618784	–68.440128	2.17	3.48	4±2	1±1	0.75	2.8±0.7	–
146†	123819.5-681830	189.581264	–68.308352	1.97	5.17	4±2	1±1	0.72	3±2	–
147†	123816.4-682213	189.568335	–68.370356	0.74	1.58	3±2	3±2	1.6	0.7±0.3	+
148†	123800.9-682226	189.503632	–68.373923	0.73	1.25	3±2	3±2	0.73	1.19±0.12	+
149†	123811.8-681934	189.549265	–68.326171	1.37	4.00	3±2	3±2	0.58	1.1±0.3	+
150†	123813.7-682608	189.557289	–68.435640	1.96	2.67	3±2	<1.1	0.72	3.6±0.5	+
151†	123815.3-681941	189.563823	–68.328264	1.37	3.92	3±2	3±2	0.57	1.69±0.17	+

Col. (1): X-ray catalogue sequence number, sorted by net X-ray counts (0.3–7 keV). Sources that were detected by `wavdetect` using a `sigthresh` of 10^{-6} but not with a `sigthresh` of 10^{-7} have been flagged with a †.

Col. (2): IAU designated source name.

Cols. (3) and (4): Right ascension and declination (in decimal degrees) for epoch J2000.0.

Col. (5): 95% confidence radius on `wavdetect` X-ray source position in arcseconds.

Col. (6): Angular offset from our derived cluster centre ($\alpha_{2000} = 12^{\rm h}38^{\rm m}07\overset{\rm s}{.}1$, $\delta_{2000} = -68°23'33''$) in arcminutes.

Col. (7): Net counts extracted in the total energy band (0.3–7 keV) with 1-σ errors.

Col. (8): Net counts extracted in the soft energy band (0.3–2 keV) with 1-σ errors. For sources CX 109, CX 111, CX 131, CX 141 and CX 150, only 1-σ upper limits are given.

Col. (9): Unabsorbed X-ray flux in the 0.3–7 keV energy band for a 2 keV MeKaL model and neutral hydrogen column of 1.9×10^{21}cm^{-2}.

Col. (10): Median energy E_{50} in keV with 1-σ errors.

Col. (11): Information about presence (+) or absence (–) of optical counterpart (details in Table 2).

Table 2. Optical Counterpart Properties

(1) CX	(2) OID	(3) Dox (″)	(4) V	(5) $B-V$	(6) Var	(7) P (days)	(8) Variable Type	(9) $L_{X,u}$ (10^{30} erg s^{-1})	(10) $\log(F_X/F_V)_u$	(11) Class
4	25708	0.23	21.65	1.27	–	–	–	25.5	0.21	CV?
7	108-058885	0.34	11.42	1.06	–	–	–	21.3	–3.96	NM
8	22375	0.18	21.10	0.77	–	–	–	16.9	–0.19	CV?
9	15550	0.45	15.458	1.150	–	–	–	14.5	–2.51	YSS
10	14106	0.11	20.40	1.88	–	–	–	11.3	–0.64	NM
12	15171	0.62	16.739	1.382	–	–	–	12.3	–2.07	SSG
13	15326	0.30	16.042	0.904	–	–	–	9.25	–2.47	AB
14	31878	1.91	20.73	1.68	–	–	–	10.4	–0.55	Unc
	31966	1.96	19.24	1.37	–	–	–	10.4	–1.14	Unc
15	29067	1.79	18.903	1.617	–	–	–	12.5	–1.20	NM
17	35116[c]	1.08	22.9[b]	–	–	–	–	9.85	0.05	Unc
	35119[c]	1.03	22.4	–	–	–	–	9.85	0.09	Unc
18	18485	0.12	14.361	0.826	V45	2.11?	EB(BSS)	8.05	–3.20	BSS
20	19384	1.40	21.79	0.6	–	–	–	9.07	–0.18	CV?
22	35113	1.51	23.3[b]	–	–	–	–	8.49	0.15	CV?
24	30048	2.37	20.37	1.03	–	–	–	6.08	–0.92	CV?
	35114[a]	2.39	23.8[b]	–	–	–	–	6.08	0.20	CV?
25	27968	1.12	16.381	1.204	–	–	–	10.3	–2.29	AB?
27	23901	0.86	16.452	1.043	V42	0.7029	EW	5.29	–2.55	AB
28	9861[c]	1.29	16.164	1.268	–	–	–	4.92	–2.70	AB
29	35093	0.32	22.5	–	–	–	–	6.04	–0.09	Unc
30	108-058907	0.36	13.11	0.53	–	–	–	4.43	–3.97	NM
31	19725	0.27	17.107	1.324	–	–	–	5.39	–2.28	SSG
36	35102	1.38	22.1	–	–	–	–	7.01	–0.17	Unc
38	12668	1.28	20.56	1.31	–	–	–	5.36	–0.90	CV?
	12714	1.75	22.0	1.1	–	–	–	5.36	–0.31	CV?
40	108-058509	0.12	13.52	0.53	–	–	–	6.65	–3.62	NM
41	8654	0.81	20.15	1.34	–	–	–	3.80	–1.22	AB?
44	4648	1.18	21.67	1.28	–	–	–	3.89	–0.60	CV?
46	21648	1.73	19.57	1.47	–	–	–	3.71	–1.46	AB
	21731	2.74	19.00	1.45	–	–	–	3.71	–1.69	AB
47	15107	0.73	19.83	1.43	–	–	–	3.53	–1.37	AB
49	11157	0.36	15.899	1.014	–	–	–	3.09	–3.01	AB
51	15544	0.30	17.558	1.116	–	–	–	3.20	–2.33	AB
53	35086	1.65	21.51	2.0	–	–	–	3.60	–0.70	NM
54	17413	1.26	21.20	1.4	–	–	–	3.39	–0.85	CV?
55	35094	1.06	17.623	0.8[e]	–	–	–	2.97	–2.33	NM
57	27290	0.43	17.563	1.027	–	–	–	3.22	–2.32	AB?
58	27108	0.38	17.744	1.422	–	–	–	3.07	–2.27	SSG
59	35095	0.39	13.75	–	–	–	–	3.33	–3.83	NM
61	15835[c]	1.27	18.38	1.29	–	–	–	2.88	–2.04	AB

continued on next page

(1) CX	(2) OID	(3) Dox (″)	(4) V	(5) $B-V$	(6) Var	(7) P (days)	(8) Variable Type	(9) $L_{X,u}$ (10^{30} erg s^{-1})	(10) $\log(F_X/F_V)_u$	(11) Class
62	26831	2.77	16.550	1.037	–	–	–	2.93	–2.77	AB?
	26933[c]	2.85	18.123	1.084	–	–	–	2.93	–2.14	AB?
63	35096	1.75	19.95	–	–	–	–	2.98	–1.40	Unc
64	35103	0.90	19.81	–	–	–	–	2.64	–1.51	Unc
	35104	0.80	19.68	–	–	–	–	2.64	–1.56	Unc
65	35117	1.31	22.8[b]	–	–	–	–	2.81	–0.52	Unc
	35118[a]	0.41	19.8	1.2	–	–	–	2.81	–1.47	Unc
67	26543	0.10	16.520	0.792	–	–	–	2.78	–2.80	BSS
68	12250	0.15	20.27	1.88	V20	0.57712	EA	2.37	–1.37	NM-AB
69	35105	3.62	22.7	–	–	–	–	2.71	–0.34	Unc
70	15446	0.36	22.3	0.9	–	–	–	3.30	–0.41	CV?
73	25282	0.57	14.028	0.893	–	–	–	2.07	–3.93	BSS
74	13995	0.39	14.606	0.876	–	–	–	2.28	–3.65	BSS
77	28170	1.58	20.97	1.9	–	–	–	2.29	–1.11	NM
78	15662	0.52	17.134	1.104	–	–	–	5.34	–2.27	AB
80	10786	2.01	19.35	1.18	–	–	–	2.31	–1.75	AB?
81	17291[a]	0.43	17.41	1.08	–	–	–	2.18	–2.56	AB
82	17610	0.21	19.19	1.26	–	–	–	1.96	–1.89	AB
83	35097	1.34	22.4	–	–	–	–	2.37	–0.50	Unc
	35098	2.40	21.13	–	–	–	–	2.37	–1.03	Unc
	35099	1.95	20.53	–	–	–	–	2.37	–1.27	Unc
85	18293	0.10	18.83	1.23	–	–	–	1.78	–2.07	AB
86	18530	0.11	15.781	0.824	V12	1.4226	EA(BSS)	1.78	–3.29	BSS
87	20540	0.16	19.50	1.48	–	–	–	1.73	–1.82	AB
88	19728	0.53	19.90	1.49	–	–	–	1.98	–1.60	AB
89	35100	0.33	18.9[d]	1.18[d]	V11	0.5405	EB/EA	1.82	–2.04	AB
91	35090	1.48	20.63	2.0	–	–	–	1.63	–1.39	NM
92	3202	2.83	20.90	0.97	–	–	–	2.26	–1.14	Unc
	3229	2.34	18.298	1.18	–	–	–	2.26	–2.18	Unc
	3251	0.77	20.37	1.27	–	–	–	2.26	–1.35	Unc
	35088	3.72	21.41	1.5	–	–	–	2.26	–0.94	Unc
	35089	3.28	21.63	1.6	–	–	–	2.26	–0.85	Unc
93	12003	0.31	17.078	1.115	V30	0.35132	EW	1.72	–2.79	AB
94	15804	0.09	16.440	1.107	–	–	–	1.56	–3.09	AB
95	21300	0.31	13.744	0.72	–	–	–	1.55	–4.17	NM
96	27916	2.28	19.93	1.28	–	–	–	1.96	–1.59	Unc
	28023	1.49	21.06	0.96	–	–	–	1.96	–1.14	Unc
97	17685	0.45	18.221	1.165	V38	1.31?	EA	1.73	–2.33	AB
100	108-058898	0.78	12.372	0.675	–	–	–	1.50	–4.73	NM
103	19794	0.19	18.714	1.120	–	–	–	1.37	–2.23	AB

continued on next page

(1) CX	(2) OID	(3) Dox (″)	(4) V	(5) $B-V$	(6) Var	(7) P (days)	(8) Variable Type	(9) $L_{X,u}$ (10^{30} erg s^{-1})	(10) $\log(F_X/F_V)_u$	(11) Class
109	17333	7.61	19.88	1.32	–	–	–	1.86	–1.64	Unc
	17434	7.47	15.175	1.384	–	–	–	1.86	–3.52	Unc
	17554	1.06	20.10	1.08	–	–	–	1.86	–1.55	Unc
	17591	1.59	21.17	1.43	–	–	–	1.86	–1.12	Unc
	17642	2.48	19.94	1.41	–	–	–	1.86	–1.61	Unc
	17683	4.41	20.77	1.04	–	–	–	1.86	–1.28	Unc
	17703	4.83	21.37	1.4	–	–	–	1.86	–1.04	Unc
	17806	7.53	20.95	1.24	–	–	–	1.86	–1.21	Unc
	35115	7.54	23.2[b]	–	–	–	–	1.86	–0.56	Unc
112	15741	0.22	19.55	1.52	–	–	–	1.40	–1.89	AB
114	35106	1.01	21.50	–	–	–	–	1.28	–1.15	Unc
115	20189	0.49	19.70	1.26	–	–	–	1.17	–1.90	AB?
119	35107	0.61	21.50	–	–	–	–	1.17	–1.19	Unc
120	20668	0.29	18.92	0.99	V34	0.37274	EW	0.96	–2.31	NM-AB
121	17091	5.45	15.585	0.999	–	–	–	1.03	–3.61	Unc
	17190	3.63	20.52	1.23	–	–	–	1.03	–1.63	Unc
	17201	4.08	20.40	1.08	–	–	–	1.03	–1.68	Unc
	17218	5.76	19.65	1.41	–	–	–	1.03	–1.86	Unc
	17219	4.99	20.63	0.87	–	–	–	1.03	–1.59	Unc
	17221	0.53	16.730	1.106	–	–	–	1.03	–3.15	Unc
	17261	4.73	20.46	0.76	–	–	–	1.03	–1.66	Unc
	35108[a]	1.56	20.43	–	–	–	–	1.03	–1.67	Unc
123	15653	0.50	14.173	1.254	–	–	–	0.91	–4.23	YSS
124	16634	0.47	19.06	1.20	–	–	–	0.87	–2.29	AB
125	17085	0.39	17.286	1.09	–	–	–	0.88	–3.00	AB?
126	17601	0.11	17.331	1.141	V13	0.37494	EW	0.86	–2.99	AB
127	28024	0.28	18.306	1.161	–	–	–	1.11	–2.49	Unc
	28109	3.88	21.55	1.4	–	–	–	1.11	–1.19	Unc
	35087	3.95	22.3	1.0	–	–	–	1.11	–0.89	Unc
128	11434	0.57	20.26	1.42	–	–	–	1.02	–1.74	AB
129	108-058613	0.20	13.07	0.72	–	–	–	0.99	–4.63	NM
130	18090	0.09	15.303	0.917	–	–	–	0.86	–3.80	BSS
131	5597	3.46	20.07	1.32	–	–	–	1.14	–1.77	Unc
	35091	3.69	22.2	1.0	–	–	–	1.14	–0.91	Unc
	35092	4.96	21.68	1.4	–	–	–	1.14	–1.13	Unc
	35109	5.71	22.1	–	–	–	–	1.14	–0.96	Unc
132	23096	0.31	14.842	0.997	–	–	–	0.93	–3.95	BSS
133	14060	0.37	19.31	1.36	V10	0.3808	EW	1.03	–2.12	AB
	14035	0.86	18.858	1.21	–	–	–	1.03	–2.30	AB
134	19489	0.76	20.54	1.61	–	–	–	0.84	–1.71	AB
135	11985	2.17	18.112	1.188	–	–	–	1.55	–2.42	Unc
	35110	0.32	22.3	–	–	–	–	1.55	–0.73	Unc

continued on next page

(1) CX	(2) OID	(3) Dox (″)	(4) V	(5) $B-V$	(6) Var	(7) P (days)	(8) Variable Type	(9) $L_{X,u}$ (10^{30} erg s^{-1})	(10) $\log(F_X/F_V)_u$	(11) Class
136	15173	0.18	15.803	0.992	V22	1.09430	EA/EB(BSS)	0.84	–3.61	BSS
137	15517	0.45	21.65	2.1	–	–	–	0.71	–1.35	NM
138	15696	0.50	17.810	1.15	V21	?	EA?	0.94	–2.76	AB
139	16576	0.18	19.04	1.14	–	–	–	0.94	–2.26	AB
142	16516	0.48	17.842	1.110	–	–	–	0.79	–2.82	AB
143	16816	1.01	20.96	1.52	–	–	–	0.68	–1.64	AB
144	22676	0.47	16.915	0.989	V24	0.35436	EW	0.70	–3.25	AB
147	18453	0.34	16.454	0.982	V25	0.40091	EW	1.43	–3.12	AB
148	15852	0.05	19.81	1.59	–	–	–	0.65	–2.12	AB
149	17650	0.63	18.962	0.72	V33	0.28997	EW	0.52	–2.56	AB
150	18031[c]	2.14	16.712	1.107	–	–	–	0.64	–3.36	Unc
151	18292	0.45	19.16	1.07	–	–	–	0.51	–2.49	CV?

Col. 1: X-ray catalogue sequence number

Col. 2: Optical source ID. For five X-ray sources, viz. CX 7, CX 30, CX 40, CX 100, and CX 129, the optical source IDs are their UCAC4 catalogue IDs. These stars were saturated in our optical images and their photometry was obtained from the UCAC4 catalogue.

Col. 3: Distance between the X-ray source and the optical counterpart in arcsec.

Col. 4: V magnitude, unless specified as B magnitude

Col. 5: $B-V$ colour.

Col. 6: Short-period binary counterpart ID from Mazur et al. (1995).

Col. 7: Period (in days) of the short-period binary counterpart.

Col. 8: Variable type, as mentioned in Mazur et al. (1995)

Col. 9: Unabsorbed X-ray luminosity (0.3–7 keV), assuming the source lies at the distance of the cluster, viz. 2.5 kpc.

Col. 10: Unabsorbed X-ray (0.3–7 keV) to optical (V band) flux ratio (2 keV MeKaL model and neutral hydrogen column of 1.9×10^{21}cm^{-2})

Col. 11: Object classification : CV? - Candidate cataclysmic variable ; AB(?) - Active binary (candidate) ; SSG - Sub-subgiant ; BSS - Blue straggler star ; Unc - Uncertain classification; NM - Non-member

Notes: *a* - photometry of the source may be dubious due to image artefacts (CX81, CX65) or low S/N ratio (CX2, CX24, CX121); *b* - the magnitude is a B magnitude; *c* - the optical counterpart lies just outside the 95% match radius, but within the 3σ match radius; *d* - value obtained from Mazur et al. (1995); *e* - B magnitude obtained from USNO B1.0 catalogue (Monet et al. 2003)

Table 3. Properties of close binaries from Mazur et al. (1995) that are matched to a *Chandra source*

(1) CX	(2) Var	(3) V	(4) $B-V$	(5) P (days)	(6) Variable Type	(7) $\log(F_X/F_V)_u$
18	V45	14.38	0.60	2.11?	EB(BSS)	–3.20
27	V42	16.37	0.98	0.7029	EB	–2.60
68	V20	20.15	–	0.57712	EA	–1.4
86	V12	15.81	0.69	1.4226	EA(BSS)	–3.3
89	V11	18.9	1.18	0.5405	EB/EA	–2.0
93	V30	17.02	0.86	0.35132	EW	–2.8
97	V38	18.2	1.16	1.31?	EA	–2.3
120	V34	18.9	1.0	0.37274	EW	–2.3
126	V13	17.29	1.00	0.37494	EW	–3.0
133	V10	19.3	–	0.3808	EW	–2.1
136	V22	15.9	0.73	1.09430	EA/EB(BSS)	–3.6
138	V21	17.74	1.20	?	EA?	–2.8
144	V24	16.84	1.1	0.35436	EW	–3.3
147	V25	16.38	0.88	0.40091	EW	–3.1
149	V33	18.24	1.09	0.28997	EW	–2.8

Col. 1: X-ray catalogue sequence number.

Col. 2: Short-period binary counterpart ID from Mazur et al. (1995).

Col. 3 and 4: V magnitude and $B-V$ colour from Mazur et al. (1995).

Col. 5: Period (in d) of the short-period binary counterpart from Mazur et al. (1995).

Col. 6: Variable type, as mentioned in Mazur et al. (1995): EA = eclipsing binary of the Algol type, EB = β Lyrae type variables with unequal minima and maxima in the light curve, and EW is a contact binary of the W UMa type.

Col. 7: Unabsorbed X-ray (0.3–7 keV) to optical (V band) flux ratio (2 keV MeKaL model and neutral hydrogen column of 1.9×10^{21} cm^{-2}).

Table 4. Comparison among old open clusters of X-ray sources with $L_X \geq 10^{30}$ erg s^{-1} (0.3–7 keV) inside r_h

Cluster	Age (Gyr)	Mass ($M_\odot$)	N_X	$N_{X,CV}$	$N_{X,SSG}$	$N_{X,AB}$	log($2L_{30}$/Mass)
NGC 6819[2]	2 – 2.4	2600	3 – 8	$\lesssim 1$	$\lesssim 1$	$\lesssim 4$	28.8–29.3
M 67[1]	4	2100^{+610}_{-550}	12	0	1	7 – 8	28.6
NGC 6791[3]	8	5000–7000	15 – 19	3 – 4	3	7 – 11	28.6 – 28.8
Cr 261	7	5800–7200	$\lesssim$26±8	$\lesssim 4$	$\lesssim 2$	2 – 23	$\lesssim$28.6 – 28.7

Col. (1): Cluster name listed in order of increasing age

Col. (2): Cluster age in Gyr

Col. (3): Cluster mass in $M_\odot$. The estimate for Cr 261 is based on the integrated V magnitude of the cluster (Sect. 3.3); for the other clusters, see the references quoted below.

Col. (4): Number of X-ray sources inside r_h with $L_X \geq 1 \times 10^{30}$ erg s^{-1}

Col. (5): Number of candidate CVs inside r_h with $L_X \geq 1 \times 10^{30}$ erg s^{-1}. M 67 does host the CV EU Cnc inside r_h, but it is fainter than the luminosity cutoff.

Col. (6): Number of candidate SSGs inside r_h with $L_X \geq 1 \times 10^{30}$ erg s^{-1}

Col. (7): Number of (candidate) ABs inside r_h with $L_X \geq 1 \times 10^{30}$ erg s^{-1}. The lower limit to the number of ABs in Cr 261 is set by CX 93 V30 and CX 147/V25, two W UMa's at a distance that is consistent with that of the cluster.

Col. (8): Ratio of the total X-ray luminosity of sources inside r_h brighter than 1×10^{30} erg s^{-1} (L_{30}), and cluster mass. The multiplicative factor 2 is included to scale the mass estimate to the half-mass radius. The value for M 67 has been updated with respect to the van den Berg et al. (2013) value, to account for an updated mass estimate (Geller et al. 2015). For NGC 6819, new membership information from Platais et al. (2011) has been included.

References – [1]van den Berg et al. (2004), Geller et al. (2015), [2]Gosnell et al. (2012), Platais et al. (2013) [3]van den Berg et al. (2013), Platais et al. (2011)

REFERENCES

Bassa, C. G., Pooley, D., Verbunt, F., Homer, L., Anderson, S. F., & Lewin, W. H. G. 2008, A&A, 488, 921

Bellazzini, M., Perina, S., Galleti, S., Federici, L., Buzzoni, A., & Fusi Pecci, F. 2008, Mem. Soc. Astron. Italiana, 79, 663

Belloni, T., Verbunt, F., & Mathieu, R. D. 1998, A&A, 339, 431

Belloni, T., Verbunt, F., & Schmitt, J. H. M. M. 1993, A&A, 269, 175

Bragaglia, A., Gratton, R. G., Carretta, E., D'Orazi, V., Sneden, C., & Lucatello, S. 2012, A&A, 548, A122

Bragaglia, A., & Tosi, M. 2006, AJ, 131, 1544

Bressan, A., Marigo, P., Girardi, L., Salasnich, B., Dal Cero, C., Rubele, S., & Nanni, A. 2012, MNRAS, 427, 127

Broos, P. S., Townsley, L. K., Feigelson, E. D., Getman, K. V., Bauer, F. E., & Garmire, G. P. 2010, ApJ, 714, 1582

Carraro, G., Girardi, L., & Chiosi, C. 1999, MNRAS, 309, 430

Chen, Y., Bressan, A., Girardi, L., Marigo, P., Kong, X., & Lanza, A. 2015, MNRAS, 452, 1068

Chen, Y., Girardi, L., Bressan, A., Marigo, P., Barbieri, M., & Kong, X. 2014, MNRAS, 444, 2525

Davies, M. B. 2015 in Ecology of Blue Straggler Stars, ed. Boffin, H. M. J., Carraro, G. & Beccari, G., 203

Dinescu, D. I., Demarque, P., Guenther, D. B., & Pinsonneault, M. H. 1995, AJ, 109, 2090

Drazdauskas, A. and Tautvaišienė, G. and Randich, S. and Bragaglia, A. and Mikolaitis, Š. and Janulis, R. 2016, A&A, 589, A50

Ebisawa, K. et al. 2005, ApJ, 635, 214

Freire, P. C. C., Hessels, J. W. T., Nice, D. J., Ransom, S. M., Lorimer, D. R., & Stairs, I. H. 2005, ApJ, 621, 959

Friel, E. D., Jacobson, H. R., Barrett, E., Fullton, L., Balachandran, S. C., & Pilachowski, C. A., 2003, AJ, 126, 2372

Froebrich, D., Schmeja, S., Samuel, D. & Lucas, P. W. 2010, MNRAS, 409, 1281

Garmire, G. P., Bautz, M. W., Ford, P. G., Nousek, J. A., & Ricker, G. R. 2003, Proc. SPIE, 4851, 28

Ge, C. and Li, Z. and Xu, X. and Gu, Q. and Wang, Q. D. and Roberts, S. and Kraft, R. P. and Jones, C. and Forman, W. R. 2015, ApJ, 812, 130

Geller, A. M., Latham, D. W., & Mathieu, R. D 2015, AJ, 150, 97

Geller, A. M., Mathieu, R. D., Harris, H. C., & McClure, R. D. 2008, AJ, 135, 2264

Giardino, G., Pillitteri, I., Favata, F., & Micela, G. 2008, A&A, 490, 113

Gilliland, R. L. et al. 1991, AJ, 101, 541

Gondoin, P. 2005, A&A, 438, 291

Gosnell, N. M., Pooley, D., Geller, A. M., Kalirai, J., Mathieu, R. D., Frinchaboy, P., & Ramirez-Ruiz, E. 2012, ApJ, 745, 57

Gozzoli, E., Tosi, M., Marconi, G., & Bragaglia, A. 1996, MNRAS, 283, 66

Güdel, M. 2004, A&A Rev., 12, 71

Hong, J., Schlegel, E. M., & Grindlay, J. E. 2004, ApJ, 614, 508

Hong, J., van den Berg, M., Schlegel, E. M., Grindlay, J. E., Koenig, X., Laycock, S., & Zhao, P. 2005, ApJ, 635, 907

Huang, R. H. H., Becker, W., Edmonds, P. D., Elsner, R. F., Heinke, C. O. & Hsieh, B. C. 2010, A&A, 513, A16

Hurley, J. R., Pols, O. R., Aarseth, S. J., & Tout, C. A. 2005, MNRAS, 363, 293

Hut, P. 1981, A&A, 99, 126

Kharchenko, N. V., Piskunov, A. E., Schilbach, E., Röser, S., & Scholz, R.-D. 2013, A&A, 558, A53

Kim, M., Wilkes, B. J., Kim, D.-W., Green, P. J., Barkhouse, W. A., Lee, M. G., Silverman, J. D., & Tananbaum, H. D. 2007, ApJ, 659, 29

King, I. R. 1962, AJ, 67, 471

Leonard, P. J. T. 1996, ApJ, 470, 521

Marshall, D. J., Robin, A. C., Reylé, C., Schultheis, M. & Picaud, V. 2006, A&A, 453, 635

Mathieu, R. D., Meibom, S., & Dolan, C. J. 2004, ApJL, 602, L121

Mazur, B., Krzeminski, W., & Kaluzny, J. 1995, MNRAS, 273, 59

McCrea, W. H. 1964, MNRAS, 128, 147

Monet, D. G. et al. 2003, AJ, 125, 984

Ottman, R., Fleming, T., & Pasquini, L. 1997, A&A, 322, 785

Pallavicini, R. 1989, A&A Rev., 1, 177

Pasquini, L., Biazzo, K., Bonifacio, P., Randich, S., & Bedin, L. R. 2008, A&A, 489, 677

Peres, G., Orlando, S., Reale, F., Rosner, R., & Hudson, H. 2000, ApJ, 528, 537

Platais, I., Cudworth, K.M., Kozhurina-Platais, V., McLaughlin, D.E., Meibom, S., & Veillet, C. 2011, ApJ, 733, L1

Platais, I., Gosnell, N.M., Meibom, S., Kozhurina-Platais, V., Bellini, A., Veillet, C., & Burkhead, M. S. 2013, AJ, 146, 43

Predehl, P., & Schmitt, J. H. M. M. 1995, A&A, 293, 889

Richer, H. B., Fahlman, G. G., Rosvick, J., & Ibata, R. 1998, ApJ, 116, L91

Röser, S., Demleitner, M., & Schilbach, E. 2010, AJ, 139, 2440

Rucinski, S. M., & Duerbeck, H. W. 1997, PASP, 109, 1340

Sandquist, E. L., Latham, D. W., Shetrone, M. D., & Milone, A. A. E. 2003, AJ, 125, 810

Skrutskie, M. F., Cutri, R. M., Stiening, R., et al. 2006, AJ, 131, 1163

Stocke, J. T, Morris, S. L., Gioia, I. M., Maccacaro, T., Schild, R., Wolter, A., Fleming, T. A., & Henry, J. P. 1991, ApJS, 76, 813

Tang, J., Bressan, A., Rosenfield, P., Slemer, A., Marigo, P., Girardi, L., & Bianchi, L. 2014, MNRAS, 445, 4287

van den Berg, M. 2013, in Astronomical Society of the Pacific Conference Series, Vol. 470, 370 Years of Astronomy in Utrecht, ed. G. Pugliese, A. de Koter, & M. Wijburg, 251

van den Berg, M., Orosz, J., Verbunt, F., & Stassun, K. 2001, A&A, 375, 375

van den Berg, M., Tagliaferri, G., Belloni, T., & Verbunt, F. 2004, A&A, 418, 509

van den Berg, M., Verbunt, F., & Mathieu, R. D. 1999, A&A, 347, 866

van den Berg, M., Verbunt, F., Tagliaferri, G., Belloni, T., Bedin, L. R., & Platais, I. 2013, ApJ, 770, 98

Verbunt 2001, å, 368, 137

Zacharias, N., Finch, C. T., Girard, T. M., Henden, A., Bartlett, J. L., Monet, D. G., & Zacharias, M. I. 2013, AJ, 145, 44

Zahn, J.-P. 1989, A&A, 220, 112